Assessment of horizontally-oriented ice crystals with a combination of multiangle polarization lidar and cloud Doppler radar

Zhaolong Wu[1, 2], Patric Seifert[2], Yun He[2, 3, 4], Holger Baars[2], Haoran Li[5, 6], Cristofer Jimenez[2], Chengcai Li[1,†], and Albert Ansmann[2]

[1]Department of Atmospheric and Oceanic Sciences, School of Physics, Peking University, Beijing 100871, China
[2]Leibniz Institute for Tropospheric Research, Leipzig 04318, Germany
[3]School of Earth and Space Science and Technology, Wuhan University, Wuhan 430072, China
[4]State Observatory for Atmospheric Remote Sensing, Wuhan 430072, China
[5]Leipzig Institute for Meteorology (LIM), Leipzig University, Leipzig 04103, Germany
[6]State Key Laboratory of Severe Weather, Chinese Academy of Meteorological Sciences, Beijing 100081, China
[†]deceased, 21 April 2025

Correspondence: Yun He (heyun@whu.edu.cn)

Abstract. The orientation of ice crystals plays a significant role in determining their radiative and precipitating effects, horizontally oriented ice crystals (HOICs) reflect up to ~40 % more short-wave radiation back to space than randomly oriented ice crystals (ROICs). This study introduces an automatic range-resolved algorithm for HOIC identification using a combination of ground-based zenith- and 15-degree off-zenith-pointing polarization lidars. The lidar observations provided high-resolution cloud phase information. The data were collected in Beijing over 354 days in 2022. A case study from 13 October 2022 is presented to demonstrate the effectiveness and the feasibility of the detection method. The synergy of lidars and collocated Ka-band cloud radar, radiosonde, and ERA5 data provide phenomenological insights into HOIC events. While cloud radar Doppler velocity data allowed the estimation of ice crystal size, Reynolds numbers, and turbulent eddy dissipation rates, corresponding environmental and radar-detected variables are also provided. HOICs were present accompanying with weak horizontal wind of 0–20 $m\,s^{-1}$ and relatively high temperature between -8 °C to -22 °C. Compared to the ROICs, HOICs exhibited larger reflectivity, spectral width, turbulent eddy dissipation rate, and a median Doppler velocity of about 0.8 $m\,s^{-1}$. Ice crystal diameter (1029 μm to 1756 μm for 5th and 95th percentiles) and Reynolds numbers (28 to 88 for 5th and 95th percentiles) are also estimated with the help of cloud radar Doppler velocity using an aerodynamic model. One interesting finding is that the previously found switch-off region of the specular reflection in the region of cloud base shows a higher turbulence eddy dissipation rate, probably caused by the latent heat released due to the sublimation of ice crystals in cloud-base region. The newly derived properties of HOICs have the potential to aid to derive the likelihood of their occurrence in output from general circulation models (GCMs) of the atmosphere.

1 Introduction

It has been recognized in the presence of Reynolds number between 1 and 100 (Pruppacher and Klett, 1996) that falling ice crystals in the atmosphere can become quasi-horizontally oriented, only slightly deviating from the horizontal alignment due to

wobbling movements. Frequently observed atmospheric optical phenomena (halos) including sun dogs (parhelia), light pillars (sun pillar, moon pillar), circumzenithal arcs, and circumhorizontal arcs, etc. require the presence of horizontally oriented hexagonal plates. Tangent arcs require horizontally oriented hexagonal columns (Liou and Yang, 2016; Saito and Yang, 2019). Both crystal types, in general described as horizontally oriented ice crystals (HOICs) can produce angle-dependent specular reflection for the incident light. The effect of that specular reflection defines the cloud radiative properties over large areas. In fact, regions with dominant HOICs can produce remarkable sunlight glints with much higher reflectance than the surroundings, as was observed by low-Earth orbit (Bréon and Dubrulle, 2004) and deep-space passive satellites (Marshak et al., 2017; Várnai et al., 2019; Li et al., 2019b).

HOICs reflect more shortwave radiation into space compared to randomly oriented ice crystals (ROICs), up to 40% more according to modeling studies (Takano and Liou, 1989), thereby significantly influencing the radiation balance (Klotzsche and Macke, 2006). Calculation shows oriented plates intercept roughly twice as much sunlight as the perfectly randomly oriented ones (Várnai et al., 2019). Stillwell et al. (2019) confirmed the significant radiation difference for HOIC and ROIC using a long-term ground-based dataset. Additionally, horizontal orientation increases the drag force from the atmosphere and thus slows the sedimentation speed of ice crystals, increasing the cloud lifetime and persistence in atmospheric models (Heymsfield and Iaquinta, 2000).

Mirror-like specular reflection also strongly influences lidar observations. When the incident light is perpendicular to the main facets of HOIC, very strong backscatter and nearly no depolarization (specular reflection at normal incidence does not rotate the plane of polarized light) are found for zenith-pointing lidar (nadir-pointing for spaceborne lidar case). However, when the incident light is several degrees off perpendicular to the surface of HOIC, a relatively weaker backscatter, and higher depolarization ratio is found for off-zenith-pointing lidar (off-nadir-pointing for spaceborne lidar case). This angle-dependent characteristic is beneficial for distinguishing the HOICs from ROICs (He et al., 2021a, b; Seifert, 2011). As another crucial feature, HOICs can lead to misclassification of the cloud phase based on the zenith/nadir polarization lidar-based cloud phase discrimination due to the similarity of the near-zero depolarization ratios produced by both, specular reflection at HOICs and backscattering from droplets of supercooled water cloud. To avoid specular reflection from HOICs, spaceborne lidars positioned several degrees off-nadir to capture the cloud phase information better, 3° for ATLID (Atmospheric Lidar) onboard EarthCARE (Earth Cloud, Aerosol and Radiation Explorer) and CALIOP (Cloud-Aerosol Lidar and Infrared Pathfinder Satellite Observations), and 2° for ACDL (Aerosol and Carbon dioxide Detection Lidar) onboard DQ-1 (Wehr et al., 2023; Hu et al., 2009; Dai et al., 2024) respectively. Many ground-based lidars and ceilometers were also positioned several degrees off-zenith to reduce the HOIC contamination of supercooled liquid droplet identification schemes (e.g., Engelmann et al., 2016).

Despite its importance, limited knowledge exists regarding HOICs. Due to the perturbation of ice orientation by the detector, it is very difficult to use airborne in-situ methods to measure the ice orientation. Remote sensing methods, including both ground-based measurement and spaceborne observations were developed and employed to investigate the characteristics of HOICs. Diattenuation, a polarization-dependent measure of scattering efficiency shown by oriented particles at so-called oblique angles, was proposed by Neely et al. (2013) to study HOICs and their radiation effects in Greenland (Stillwell et al., 2019). Seifert (2011) used zenith-pointing polarization Raman lidar to retrieve the lidar ratio of HOICs and pointed out that

HOICs show a lower lidar ratio than supercooled water clouds. Westbrook et al. (2010) used the ratio of backscatter (color ratio) from an off-zenith pointing ceilometer and a zenith-pointing Doppler lidar to identify and study the HOICs, though his study lacked depolarization ratio capacity. He et al. (2021a), with a 30 ° off-zenith lidar along with a zenith-pointing lidar, used the enhanced volume depolarization from off-zenith-pointing lidar as a feature to identify HOICs, and found the horizontal ori-
60 entation can form from a continuously descending ice cloud layer. However, they did not use the backscatter as a restraint and his identification method was manual. CALIOP separated HOIC from ROIC and liquid water cloud based on layer-integrated attenuated backscatter and depolarization ratio threshold (Hu et al., 2009). With its global coverage, CALIOP shows a powerful advantage in observing the global distribution of HOICs. However, lidar attenuation when a liquid-water-topped cloud exists could lead to an underestimation of the HOICs fraction. The relatively coarse spatial resolution and layer-integrated,
65 vertically homogeneous (within a determined cloud layer) official cloud phase classification (Hu et al., 2009) is not detailed enough to investigate the horizontal orientation. The spaceborne lidar is more suitable for global-scale statistics, providing only a snapshot observation, which cannot observe the process-level evolution of HOIC. Passive satellites using glint to identify HOICs can provide the macroscopic distribution of oriented ice (Marshak et al., 2017; Bréon and Dubrulle, 2004), but without height-resolved information.

70 Fundamental questions such as about the frequency of HOIC still persist, literature provides different results as a consequence of the variability of the underlying detection and counting methods: profile-based (Ross et al., 2017), range-bin-based (Westbrook et al., 2010; Sato and Okamoto, 2011), cloud-layer-based (Zhou et al., 2012a; Saito et al., 2017), or area-based (Bréon and Dubrulle, 2004; Marshak et al., 2017). Westbrook et al. (2010) points out that many of the results from different studies are inconsistent. Noel and Chepfer (2010) found 6% optically thin ice cloud contains oriented ice using nadir-pointing
75 CALIPSO data. Zhou et al. (2012b) estimated HOIC exists in approximately 60% of optically thick ice and mixed-phase cloud layers. Marshak et al. (2017) pointed out that roughly every third DSCOVR/EPIC image (see http://epic.gsfc.nasa.gov) shows a sunglint over land, which is most likely due to HOICs. The automated algorithm proposed in this paper can serve as a good starting point for future HOIC frequency and percentage studies.

More observations with HOIC-identification capabilities are needed to improve the assignment of the orientation of ice
80 hydrometeors in the cloud parameterization schemes, which is usually not considered in current general circulation models or radiative transfer models (Klotzsche and Macke, 2006; Zhou et al., 2012b). Due to the latitude-dependent HOIC occurrence (Noel and Chepfer, 2010), the long-term observation at midlatitude stations like Beijing (116.3°E, 40.0°N), China is essential to help understand the orientation phenomenon.

Previous ground-based statistics are mostly case studies describing areas with specular reflection effects, lacking precise
85 height-resolved bin-level observations and products. Compared to spaceborne observations, the ground-based dual-angle-lidar scheme has a higher spatial and temporal resolution to analyze the evolution of HOICs, which is beneficial to our understanding of the process. It gives us a more comprehensive understanding of the environmental characteristics of the emergence of HOICs. In addition, simultaneous cloud radar observations, which very few HOIC studies utilized so far, can obtain Doppler velocities, which help us to estimate ice crystal size information, and to derive turbulence information which helps to understand under
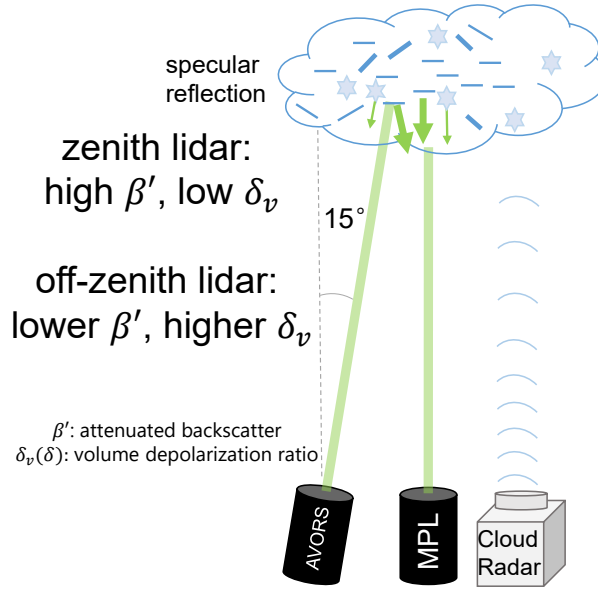90 which conditions HOICs tend to form.

Figure 1. Schematic figure of the two lidars and the zenith-pointing cloud radar, which were used in the framework of this study.

The simultaneous observations using ground-based zenith and 15 degrees off-zenith-pointing polarization lidars along with cloud radar (see Fig. 1) were conducted to study HOIC in Beijing, China over 354 days in the year 2022. This article proposes an automatic algorithm for HOIC detection based on dual-angle polarization lidar observations and then explores the potential of such a unique system using collocated cloud radar, radiosonde and ERA5 data. The article is structured as follows. Section 2 presents the instruments and data used. In Sect. 3, we detail the methodology employed to detect the cloud bins and then identify HOICs. Next, a case study is shown in Sect. 4. Finally, conclusions are drawn in Sect. 5.

2 Instruments and data

We propose a new and unique set of instruments to study HOIC occurence and formation: 2 polarization lidars with different zenith angles, Doppler cloud radar. The depolarization ratio measured by zenith-pointing MPL and 15° off-zenith-pointing AVORS lidar was calibrated using well-calibrated Raman lidar as a reference, as is described in details in Appendix B2.

2.1 MPL

A Micro Pulse Lidar (MPL; Model MPL-4B-IDS-532-AT) manufactured by Sigma Space Corporation has been continuously operated since 2016 (Chu et al., 2019; Xu et al., 2020; Chang et al., 2021), at zenith angle on the roof of the Peking University (PKU) Physics Building (116.3°E, 40.0°N, ~40 m above sea level). The temporal and vertical resolution of the MPL are 15 s and 15 m, respectively, and the blind zone is 195 m (Welton and Campbell, 2002). The pulse repetition frequency is 2500 Hz,

and the pulse energy is 6–8 μJ. The MPL is a single-wavelength (532 nm) elastic polarization lidar with a field of view (FOV) of 0.1 mrad. By using the actively controlled liquid crystal retarder (LCR), the MPL achieves polarization detection capabilities by using only one detector for the two polarization channels (Flynna et al., 2007). The MPL was placed in a container with air conditioning to maintain stable observations. On top of the container, there is a slightly tilted glass to guarantee that lidar observations are not interrupted by bad weather. A lens hood above the glass reduces the sunlight noise. Maintenance staff carefully wipe the glass above the lidar container every day to minimize attenuation caused by rain and aerosol deposits. Unless otherwise stated, the time in the paper is local time (LT, UTC+8).

2.2   AVORS lidar

An off-zenith-pointing lidar (Model Portable Particle Lidar, http://en.avorstech.com/product/670.html) manufactured by AVORS Technology has been continuously operating since 2022 (Sun et al., 2024). The AVORS lidar was placed 5 meters away from the MPL on the same roof. The AVORS lidar is a single-wavelength (532 nm) elastic polarization lidar, with a rotatable base and an electric motor to change its zenith and azimuth angle. The laser beam of the AVORS lidar was placed 15 degrees off the zenith (towards the north to reduce the possible sunlight noise to the greatest extent) to avoid specular reflection during our study. The pulse energy is 20 μJ with the pulse repetition frequency of 2500 Hz, and the FOV of the telescope is 0.2 mrad. The temporal and vertical resolution of the AVORS lidar data are 10 s or 60 s (adjustable, most of the time 60 s in this research) and 15 m respectively, and the blind zone is 45 m. Technical specifications of the lidar system are listed in Table A1. Note, the AVORS lidar has two Photomultiplier Tube (PMT) detectors for each polarization channel (Fig. A1). In the following analysis, the height of observations from the AVORS lidar of was calculated as $\cos(\frac{\pi}{12})$ times the range from the lidar. The AVORS lidar was installed outdoors and the temperature was maintained by its own air conditioning system integrated inside the lidar. Due to the lack of containers or lens hoods, the lidar signal is slightly more contaminated by sunlight noise in the daytime, resulting in a relatively lower signal-to-noise ratio (SNR). Furthermore, the AVORS lidar was zenith-pointing from 9 May 2023 to 3 June 2023, during this period the depolarization ratio for cloud could be compared with MPL (Fig. B2).

The uniqueness of the 15° off-zenith angle observation is valuable in this research. Previous research shows that the 3° off-nadir angle of CALIOP was not sufficient to completely eliminate the effects of specular reflections (Noel and Chepfer, 2010; Kikuchi et al., 2021), hence CALIOP possesses the ability to offer a product about oriented ice at the 3° off-nadir angle. Also, ground-based polarization lidar with 4° or 5° off-zenith-pointing angle can also sometimes show specular reflections (Tansey et al., 2023; Seifert et al., 2011). The 30° off-zenith angle of He et al. (2021a) used is too large, and there will be a large horizontal offset at high altitude. In this study, a 15° off-zenith angle is a moderate angle, while avoiding the backscatter specular reflection of HOICs as much as possible, and also trying to ensure that the same cloud can be seen by both lidars.

2.3   Raman lidar

Portable, eye-safe lidars, such as MPL and AVORS, have polarization capabilities. Preliminary results revealed that the calibration of the systems needs to be improved in order to make the collocated measurements comparable. A well-characterized lidar was used as a reference to characterize the two micropulse lidar systems. A Raymetrics Raman lidar (Model LR231-D300) at

the same campus (about 360 m away from MPL and AVORS lidar) was employed as the reference for the depolarization ratio (Li et al., 2016, 2019a; Tan et al., 2019, 2020a, b; Ren et al., 2021). The Raman lidar operates at three wavelengths (355, 532, and 1064 nm), two of them 355, 532 nm are equipped with polarization channels. In the present study, the 532 nm channel of this Raman lidar has been designated as a reference for the calibration of the depolarization ratios of the other two lidars (see B2 in detail). Its performance of depolarization measurement has been verified by several previous studies (Tan et al., 2020a, b). The $\Delta 90$ method was employed to ensure its accuracy for depolarization ratio (Freudenthaler et al., 2009). Note that we do not use this Raman lidar for HOIC identification due to its discontinuous observation.

2.4   Cloud radar

To further explore the potential of the new approach in the investigation of HOIC events, additional information from a radar instrument was considered. The larger wavelength of the radar instrument makes it able to penetrate deeper into clouds compared to lidar, it is also more sensitive to large hydrometeors. The Doppler spectrum provides an estimation of the falling velocity of particles, which allows us to estimate the particle size using aerodynamic models. The radar measurements were also used to derive turbulence-related information, such as turbulent eddy dissipation ratio (EDR) and Reynolds number (see Appendix D and E), which may play a significant role in the orientation of ice crystals. To our best knowledge, no Doppler cloud radar data are used to investigate the identified horizontally oriented ice except for Westbrook et al. (2010) and Stillwell et al. (2018), so it provides a unique chance to investigate more radar-based characteristics for different orientation behaviors of ice crystals.

A 33.44 GHz Ka-band solid-state, depolarization, multi-mode, zenith-pointing millimeter-wave cloud radar (MMCR, Model HMB-KP) manufactured by Beijing Institute of Radio Measurement has been continuously operating at Peking University since 2018 (Wang et al., 2022; Zhang et al., 2024). The cloud radar is placed 5 meters beside the MPL container. The temporal resolution is about 13 s (adjustable), and the vertical resolution is 30 m. The radar operates in four alternating modes: boundary layer mode (mode 1), cirrus mode (mode 2), precipitation mode (mode 3), and middle-level mode (mode 4) (Ding et al., 2022). These four modes vary in pulse compression ratios and numbers of both coherent and incoherent integrations. The boundary layer mode is designed to identify low-altitude clouds by utilizing a narrower pulse waveform and increasing the number of coherent integrations to enhance detection capability. In the cirrus mode, pulse compression techniques are employed to boost sensitivity for detecting high-altitude clouds with weaker radar echoes. The precipitation mode features an extended unambiguous range and velocity measurements tailored for observing rainfall. The middle-level mode similarly applies pulse compression techniques but with a reduced number of coherent integrations. Furthermore, there is one combined mode (mode 8) that combines all the modes to produce one final observation result, which we use in this research. The radar measurements contain raw data of Doppler spectra and spectral moments including reflectivity, mean Doppler velocity, spectrum width, and linear depolarization ratio. The minimum detectable reflectivity factor of this radar is -40 dBZ. Compared to lidars, radar exhibits greater sensitivity to larger particles (Westbrook et al., 2010; Bian et al., 2023). However, this Ka-band cloud radar may fail to detect certain tiny liquid droplets and optically thin ice clouds.

2.5 Radiosonde and ECMWF ERA 5 reanalysis data

Radiosondes were launched every day at 00:00 UTC (08:00 local time) and 12:00 UTC (20:00 local time) at the Beijing Nanjiao meteorological site (116.47°E, 39.80°N, WMO NO. 54511), 25 km from our lidar site (Chu et al., 2019), providing meteorological parameters, e.g., temperature, relative humidity, and horizontal wind speed and direction. As a measure to compensate for the time sparsity of the radiosonde, ECMWF ERA5 reanalysis from the grid point of PKU (116.3°E, 40.0°N) was used to provide the meteorological parameters, i.e., the temperature, wind, and relative humidity over ice. ERA5 reanalysis data for 2022 were compared with simultaneous radiosonde profiles, as in Yin et al. (2021)., and the difference in temperature, wind speed, and relative humidity are 0.2 ± 0.86 °C, 0.53 ± 1.98 m s^{-1}, and -5.46 ± 12.69 %, respectively, indicating reliability of ERA5 data for our analysis.

3 Methodology

This section introduces a new identification scheme and describes the analysis procedure. First, raw lidar data were calibrated to obtain attenuated backscatter coefficient (see Appendix B1). Second, lidar, cloud radar, and ERA5 data were re-gridded (averaged or interpolated) to 5 min× 15m resolution. Then the following algorithms and corrections were applied to get the HOIC and other hydrometeor types.

3.1 Cloud layer identification algorithm

An advanced value distribution equalization method (Zhao et al., 2014) was applied to identify cloud bins from lidar backscatter signals. Next, the overlap region of the cloud bins detected by both MPL and AVORS lidars was selected for the further cloud phase determination algorithm. For HOIC cases, zenith-pointing lidar observations have a much stronger backscatter than off-zenith-pointing lidar observations. The identification of cloud bins mainly depends on the backscatter, the cloud detection algorithm can identify one range bin as a cloud at least when the backscatter of the bins reaches a predefined threshold whose determination is explained by Zhao et al. (2014). The limitation of the cloud detection algorithm to those regions where the signals of both lidars overlap will lead to an underestimation of some upmost HOIC range bins (beyond the off-zenith lidar attenuation region but still clear on zenith lidar observation, compare Figs. 4a, c, and g).

It is essential to evaluate whether the two lidars detect the same cloud layer by estimating the typical horizontal deviation of the two laser beams at cloud height. For a cloud at an altitude of 6 km, the horizontal deviation from the zenith-pointing lidar is $6 \text{ km} \times \tan(\frac{\pi}{12}) = 1.6$ km. Assuming a horizontal wind speed is $v = 20$ m s^{-1} (see radiosonde Fig. 6b) and the wind direction is along the line between the scattering volumes of the two angle lidars, the horizontal movement of the cloud is 6000 m within five minutes, which is the temporal resolution utilized in data processing. Consequently, if both lidars observe the same cloud within the same time slot (> 5 min), the horizontal deviation of the off-zenith pointing lidar is less significant (1.6 km < 6 km). Although with increasing height, the horizontal distance between the probed volumes also increases (from 0.268 km at 1 km height to 2.68 km at 10 km height). In reality, the wind direction does not always align with the line connecting the scattering

volumes of the two-angle lidars. Therefore, we must assume horizontal homogeneity of the detected cloud layers over a certain lateral scale. This assumption is likely valid for horizontally homogeneous stratiform clouds. However, caution is needed for discrete, small-scale clouds, as misalignment may occur.

3.2 Cloud phase determination algorithm

A specialized algorithm (Fig. 2) is applied to differentiate between different cloud phases for the intersecting cloud bins observed by both lidars. First, we utilized the temperature of homogeneous nucleation ($<-38°C$) to distinguish the ice phase, followed by using the off-zenith-pointing lidar volume depolarization ratio of 0.1–0.3 to identify ice-containing cloud bins at temperatures between 0 and $-38°C$. Cloud bins with a volume depolarization ratio of ≥ 0.3 are categorized as randomly oriented ice crystals (ROICs). Cloud bins with a volume depolarization ratio of 0.1–0.3 are categorized as mixed-phase cloud bins (MPCs). If the cloud parts categorized as ROICs or MPCs have $\delta_{\text{off-zenith}} > 0.1$ and $\delta_{\text{zenith}} < 0.1$, then we used the zenith-to-off-zenith ratio of attenuated backscatter > 2 and the zenith-to-off-zenith ratio of volume depolarization ratio < 0.6 as stringent criteria to exclusively capture the most representative signals of HOIC, since the specular reflection effect is strong enough without ambiguity. On the contrary, ice-containing bins that do not meet the three thresholds are categorized as ROICs or MPCs. It should be mentioned that the real case of the orientation of the ice crystals is always a mixture within a lidar-detected bulk (Saito and Yang, 2019; Borovoi et al., 2018). This means that the HOIC label indicates the specific range bin contains HOIC (with a certain proportion) which produces an unambiguous specular reflection signal; however, some ROICs may still exist in the range bin.

The threshold values were fixed empirically from the whole cloud dataset collected during 2022 (Seifert, 2011; Lewis et al., 2020; Whitehead et al., 2024). The criteria used to select a typical HOIC bin are shown in Fig. 3. Figure 3a is the median volume depolarization ratio as a function of temperature for all detected cloud layers in 2022. The depolarization ratio δ indicates particle sphericity: ROICs show a higher volume depolarization ratio on the order of 0.3–0.5, while spherical liquid droplets have near-zero values (Ansmann et al., 2008; Seifert, 2011). A high depolarization ratio (> 0.3) at temperatures below $-38\ °C$ (the threshold temperature for homogeneous freezing) and a low depolarization ratio (< 0.1) at temperatures above $0\ °C$ are identified as the depolarization ratio criteria for ice and liquid water clouds, respectively. The two depolarization ratio threshold values are shown in red dashed line in Fig. 3a. Zenith lidar shows much lower depolarization than off-zenith lidar between $-40\ °C$ and $0\ °C$, probably due to contamination of the data by HOICs. Figure 3b shows the ratio of attenuated backscatter and depolarization ratio by means of a density scatter plot which is based on all cloud bins detected in 2022. Most cloud bins accumulate around the 1:1 line, indicating that zenith and off-zenith lidar have comparable volume depolarization ratio and attenuated backscatter. In contrast, a distinct tail-like cluster is evident in the upper-left region of Fig. 3b. The lower depolarization and higher backscatter in zenith lidar observations compared to off-zenith lidar observations shown in this cluster are clear features of HOICs. For the identification scheme, we use the zenith-to-off-zenith ratio of the attenuated backscatter ratio greater than 2 and depolarization ratio less than 0.6 as criteria to avoid the most frequent cloud bins (green, yellow, and red) in the center part of Fig. 3b. This is a relatively strict criterion as it considers both the criterion for attenuated backscatter and depolarization ratio to categorize the most representative bins for specular reflection. In the case of liquid-water clouds, the

zenith-to-off-zenith depolarization ratio differs from 1, ranging between 0.55 and 1 according to (Jimenez et al., 2020) as the ratio of lidar FOVs is 1:2. However, the backscatter ratio will be less than one, making the distinction of HOICs unambiguous with the described criteria.

240 Figure 3c shows the density scatter plot between off-zenith lidar's attenuated backscatter and depolarization ratio. Two evident clusters can be found: low depolarization ratio and high backscatter indicating liquid water clouds and high depolarization ratio and low backscatter indicating ice clouds, respectively. Nonspherical ice crystals exhibit higher δ_v compared to spherical liquid water droplets, whereas droplets have higher β' due to their higher concentration. The black dashed lines ($\delta_v < 0.1$ and $\beta' > 5$ Mm^{-1}sr^{-1}) indicate the criteria for the classification of liquid water. If a cloud bin meets the two introduced criteria

245 and has a temperature ≥ 0 °C, it is categorized as liquid water (or water as an abbreviation). If the temperature is below 0 °C, it is then flagged as a supercooled liquid water cloud (SWC). Note that if a cloud bin meets a relatively low depolarization ratio ($\delta_v < 0.1$) but does not meet the attenuated backscatter criterion ($\beta' \leq 5$ Mm^{-1}sr^{-1}), it is classified as non-typed cloud bins (similar to Baars et al., 2017). This usually happens when the concentration of cloud particles is low or the range bins are actually some dense aerosol particles (e.g. mineral dust). Discriminating optically-thin clouds and dense aerosol is still a

250 challenge for a cloud mask algorithm based on lidar backscatter signal, thus we exclude the non-typed cloud bins from further analysis in this study.
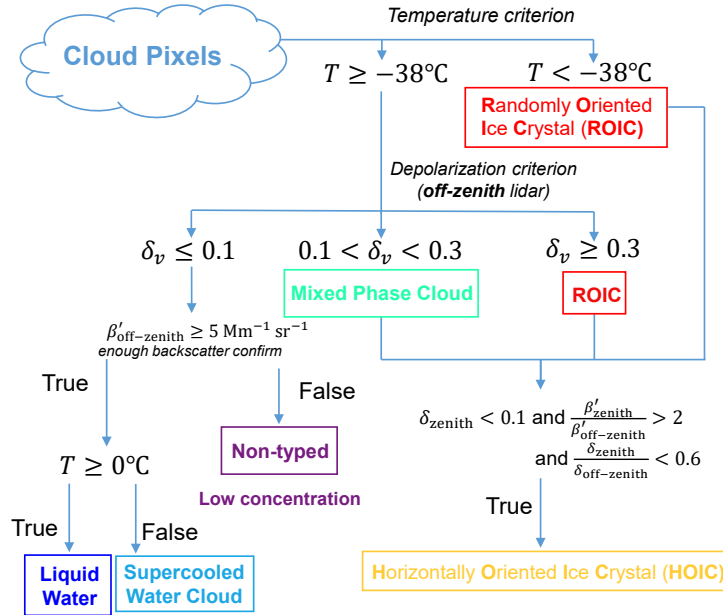

Figure 2. Flowchart of the algorithm for the classification of hydrometeor types.
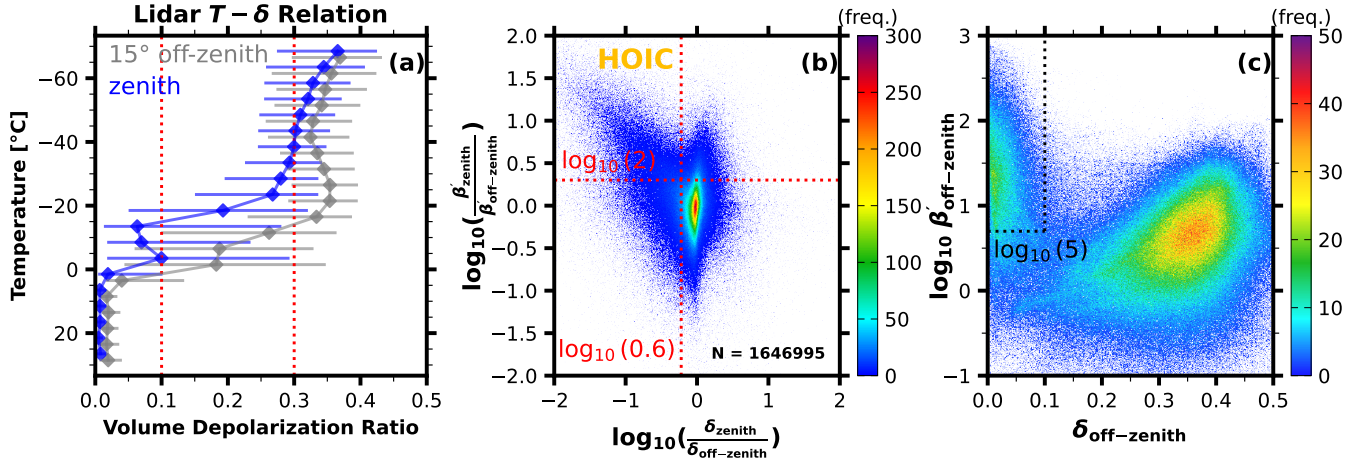
Figure 3. Definition of criteria for identification of the HOICs (red dashed lines). All subfigures were created using all the cloud bins observed in 2022. **(a)** Median volume depolarization ratio as a function of temperature for each height bin within all detected cloud bins in temperature increments of 5 °C. Horizontal bars indicate the interquartile range (IQR). **(b)** Density scatter plot of the ratio of zenith- to off-zenith-pointing lidar's volume depolarization and attenuated backscatter, $\log_{10}$ scale. **(c)** Density scatter plot of volume depolarization ratio and attenuated backscatter (unit in $\mathrm{Mm^{-1}sr^{-1}}$, $\log_{10}$ scale) for off-zenith-pointing lidar. Black dashed lines indicate the criteria used for the identification of liquid water.

3.3 Cloud phase correction

After applying the cloud phase discrimination algorithm, the potential multiple scattering effects and the contamination of the molecular depolarization ratio for ice clouds have to be considered, thus the following two corrections were conducted.

3.3.1 Typing correction above liquid layers

The off-zenith lidar, with its greater FOV (0.2 mrad compared to 0.1 mrad), generally results in a higher depolarization ratio at the top of water clouds than the zenith-pointing MPL (see Fig. 3a, T > 0°C region). This occurs when the effect of multiple scattering is pronounced as it penetrates the water cloud. Due to the different deadtime reactions for the two lidar detectors, MPL shows stronger attenuated backscatter at low altitudes (< 1.2 km). We thus categorized HOIC bins below 1.2 km as liquid water cloud (T ≥ 0 °C) or supercooled liquid water cloud (T < 0 °C). For water clouds above 1.2 km, if the topmost 100 meters of a profile have been flagged as HOIC but the layer shows liquid water towards the bottom, the upper bins will be classified as liquid water. This criteria allows us to exclude possible artifacts led by horizontal homogeneities and strong attenuation of the laser beam in the liquid cloud layer. In this way, this method conservatively corrects most misclassified HOICs at the top of water clouds back to the water phase.

3.3.2 Ice virga correction beneath pure ice clouds

As the elastic backscatter lidars we used for our study lack Raman or high spectral resolution channels, we use the volume depolarization ratio instead of the particle depolarization ratio, to avoid the introduction of additional uncertainties by the assumption of lidar ratios in the Klett-Fernald method (Fernald, 1984) that would be required for calculation of the ratio of particle to molecular backscattering. Application of the volume depolarization ratio however introduces certain ambiguities within thin clouds or in presence of low concentrations of ice crystals, as it is the case, e.g., in the ice virga region beneath pure ice clouds. The reason is, that the magnitude of the volume depolarization ratio depends on the relative contribution of the molecular depolarization ratio which is caused by backscattering at air molecules (Cairo et al., 1999). With the decreasing contribution of particle backscattering, the molecular backscattering and the associated low depolarization ratio of 0.004 (in the case of AVORS lidar) contaminates the total signal and decreases the effective volume depolarization ratio of the ice crystals, resulting in the ice bin not reaching the depolarization-ratio criteria of 0.3 for the off-zenith-pointing AVORS lidar. This leads to them being categorized improperly as mixed-phase cloud bins, even though actually no water droplet may exist under this circumstance. For MPC bins near the bottom of a cloud, the following procedure was thus applied. If more than 5 out of the 10 adjacent cloud range bins above an MPC cloud bin contain ROICs, and the temperature is below $-20\,°C$, they are re-categorized as ROICs. The threshold of $-20\,°C$ is a typical criterion for the sharp decrease of the fraction of supercooled liquid water (Yorks et al., 2011; Wang et al., 2019), even though a small likelihood for the presence of liquid water persists down to $-38\,°C$ (see, e.g., Radenz et al. (2021) and Fig. 4g), 20:00 to 21:00 at heights above the $-22\,°C$ isotherm.

4 Case study on 13 October 2022

Figure 4 illustrates a case study of a mid-level cloud layer from 13 October 2022, when strong specular reflections were observed with the zenith-pointing lidar for almost the whole day. A high backscatter and low depolarization ratio in the zenith-pointing lidar observations and much lower backscatter and higher depolarization in the off-zenith-pointing lidar measurements indicated the presence of HOICs. The HOIC flag as derived by the algorithm introduced in this study is denoted in orange in Fig. 4g. Figure 5 shows average profiles of selected lidar and radar parameters for the period from 11:00 to 12:00 (local time) on 13 October 2022. The attenuated backscatter coefficient of HOIC (yellow shaded region) observed by zenith-pointing lidar is nearly two orders of magnitude larger than that observed by the off-zenith-pointing lidar (Fig. 5a). The volume depolarization ratio from the zenith-pointing lidar is nearly zero, while for the off-zenith lidar observation, the peak volume depolarization ratio exceeds 0.3 (Fig. 5b). Additionally, Fig. 5c and d, respectively, illustrate that the radar reflectivity factor is greater for HOIC while Doppler velocity is smaller, compared to ROIC.

This HOIC event persisted for nearly the whole day. Some HOIC bins showed strong attenuated backscatter for the zenith-pointing lidar but relatively lower attenuated backscatter for the off-zenith-pointing lidar. Still, between 00:00 and 03:00 such bins were not identified as cloud, probably because the backscatter observed by the off-zenith-pointing lidar was too small for triggering the cloud mask detection for the off-zenith-pointing lidar. This demonstrates the stringency of the cloud identification criterion of the HOIC detection algorithm.
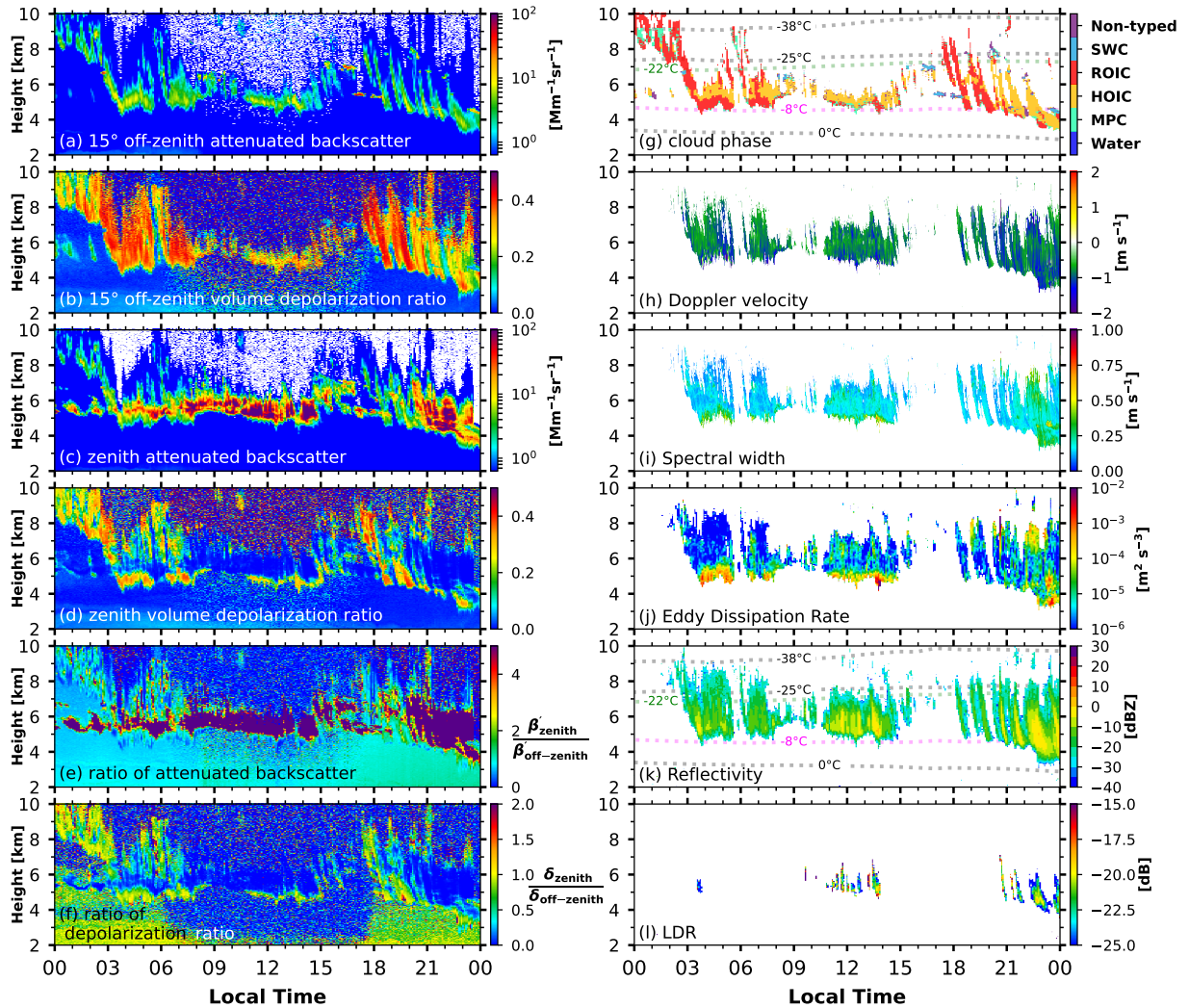
Figure 4. Lidar ((**a**)-(**g**)) and zenith-pointing Ka-band cloud radar ((**h**)-(**l**)) observations on 13 October 2022, time-height contour plots (5 min / 15 m resolution for (**a**)-(**g**), 13 s / 30 m resolution for (**h**)(**i**) to show the variation of Doppler velocity, 5 min / 30 m for (**j**)-(**l**)). (**a**) 15 ° off-zenith-pointing lidar attenuated backscatter. (**b**) 15 ° off-zenith-pointing lidar volume depolarization ratio. (**c**) Zenith-pointing lidar attenuated backscatter. (**d**) Zenith-pointing lidar volume depolarization ratio. (**e**) The ratio of attenuated backscatter for zenith-pointing and off-zenith-pointing lidar. (**f**) The ratio of volume depolarization ratio for zenith-pointing and off-zenith-pointing lidar. (**g**) Cloud phase categorization results with isotherm from ERA 5 data. Abbreviations of SWC, ROIC, HOIC, and MPC represent supercooled liquid water cloud, randomly oriented ice crystal, horizontally oriented ice crystal, and mixed-phased cloud. There is no cloud bin categorized as (warm) water due to the subzero temperature. (**h**)(**i**)(**k**)(**l**) Cloud radar detected momentum data: Doppler velocity, spectral width, reflectivity (with isotherm from ERA 5 data), and linear depolarization ratio (LDR). (**j**) Cloud radar retrieved eddy dissipation rate (EDR, ϵ).
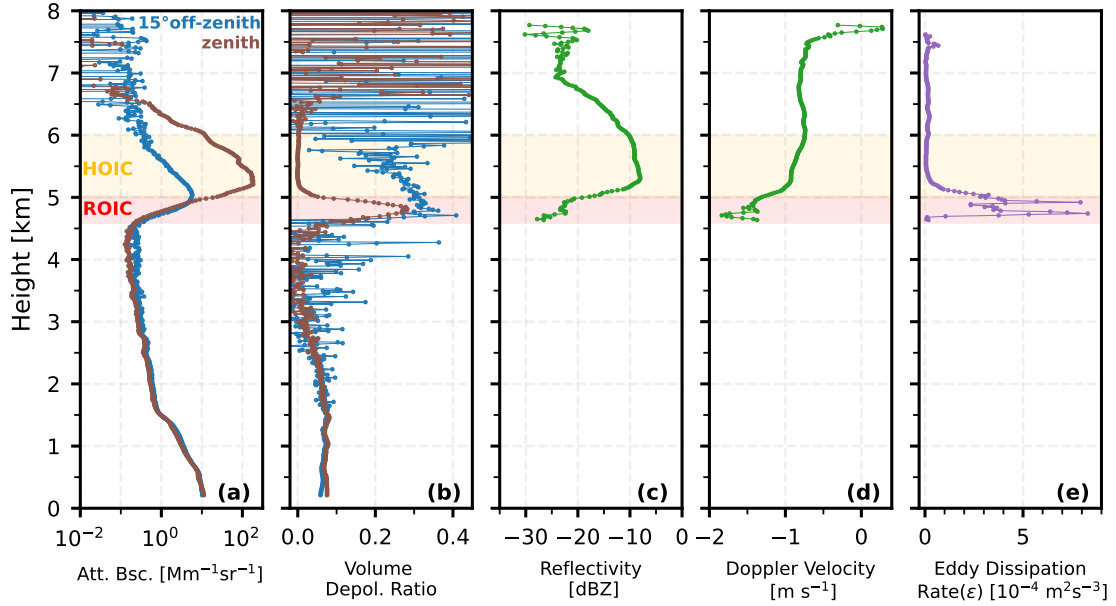
Figure 5. Lidar **(a-b)** and radar **(c-d)** observations at 11:00-12:00 on 13 October 2022; **(a)** shows the attenuated backscatter profiles from both zenith and off-zenith pointing lidars. **(b)** shows the volume depolarization ratio from both lidars. **(c)** and **(d)** show the radar reflectivity and Doppler velocity, respectively.**(e)** Retrieved eddy dissipation rate. The shadowed orange regions denote the presence of HOICs, and the red regions represent the dominance of ROICs.

4.1 General description of a HOIC event

It is noteworthy that zenith lidar observations for some regions show a high depolarization ratio below the cloud levels of strong specular reflection. Prominent time-height regions where this was the case, are for instance the time periods from 03:00–08:00 and from 11:00–15:00 at the height level of 4–5 km. This phenomenon is described as the 'switch-off' of the specular reflection conditions (Westbrook et al., 2010; He et al., 2021a). Having the observations of both depolarization lidars and Doppler cloud radar available, this study aims to zoom in on this phenomenon in more detail than was done in previous studies. The cloud radar observations (Fig. 4) show that the Doppler velocity changes significantly with time at the cloud base of the high-depolarization regions at the cloud base (compare Figs. 4d and 4h). The zenith lidar observation's high depolarization ratio region also coincides with a relatively higher spectral width of Doppler velocity (Fig. 4i). A higher spectral width usually means stronger turbulence, more complex particle spectral distributions, stronger wind shear, beam broadening within the region, etc (Kollias et al., 2007). In order to separate the effect of turbulence from other factors affecting spectral width, the turbulent eddy dissipation rate (EDR, ϵ) was computed to reflect the turbulence (Figs. 4j and 5e) using quantities including the standard deviation of Doppler velocity and horizontal wind speed. Details on the EDR retrieval are outlined in Appendix E. Measuring the turbulent kinetic energy (TKE) dissipation rate, or turbulent eddy dissipation rate, which represents the rate of conversion
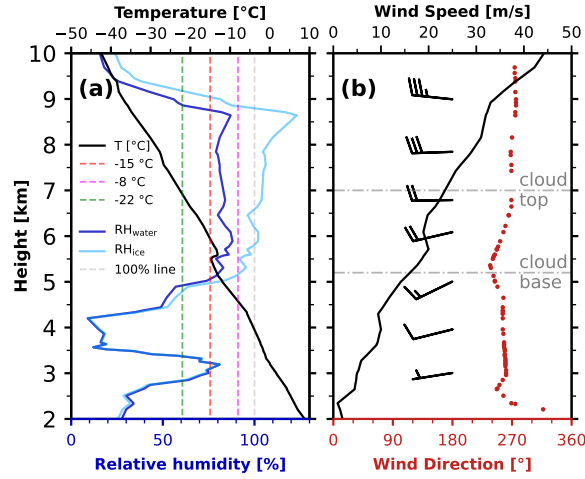
13

Figure 6. Beijing Nanjiao radiosonde profile (25 km away from PKU) at local time (UTC+8) 08:00 on 13 October 2022. **(a)** Temperature (black) and relative humidity with respect to liquid (deep blue) and ice (light blue) profile; **(b)** Wind speed (black), wind direction (red), and wind barbs. Two gray horizontal dash-dotted lines represent the cloud base, approximately 5.2 km, and the cloud top, around 7 km, respectively.

of TKE into heat or the rate at which the TKE is dissipated by viscosity, is a good way to estimate the turbulence activity. As a quantitative proxy of atmospheric turbulence, a large EDR indicates rapid energy dissipation and high atmospheric turbulence (Griesche et al., 2020). The high δ_v region above the cloud base (Fig. 5b, brown line within red shaded region, also see Fig. 4d) in the zenith lidar observation has a higher eddy dissipation rate (Fig. 5e, also see Fig. 4j), suggesting that the strong turbulence may be linked to latent heat release from the sublimation of ice crystals near the cloud base. Another possible explanation is that this stronger turbulence in return causes the break up of the ice crystal orientation. Horizontally oriented ice crystals need calm dynamic conditions and low turbulence to maintain their quasi-horizontal orientation (Klett, 1995; Garrett et al., 2015).

The following subsections analyze the environment variable, cloud radar observed variables, and diameter and Reynolds numbers retrieved for HOICs. Then, the relationship between supercooled water clouds and the different orientations of ice crystals is discussed.

4.2 Environment variables

Figure 6 shows the measurements of a radiosonde that was launched at Beijing Nanjiao station at 08:00 LT on 13 October, including the temperature and relative humidity, and the horizontal wind speed and direction profile. The temperatures of $-8\,°C$, $-22\,°C$ and $-15\,°C$ are denoted using magenta, green and light red dashed lines, respectively. Between temperatures of $-8\,°C$ and $-22\,°C$ plate-like ice crystals tend to form, according to the ice crystal habit diagram, i.e. morphology of ice crystals as a function of temperature (Libbrecht, 2005; Li, 2021; Bailey and Hallett, 2009). Overall, the highest probability for the occurrence of HOIC was reported to occur at the temperature level of $-15\,°C$ (Westbrook et al., 2010). In Fig. 6a,

the temperature for typical specular reflection (between 5 and 7 km) is around -15 °C, which falls within the plate-like ice
crystal temperature range of -22 °C to -8 °C, while the relative humidity over ice (Fig. 6a, light blue line) approaches or
slightly exceeds 100%. As seen from Fig. 6b, the wind was western and relatively light (approximately 10–20 m s^{-1}) at the
altitudes of the HOIC layer, which is beneficial for HOIC to maintain. Since the horizontal orientation is quasi-horizontal with
some fluttering or wobbling angle, an increase in horizontal wind speed may impinge upon the principal facet of the HOIC,
generating significant torque that could potentially disrupt their orientation. Figure 6b also shows the wind speed and direction
of the cloud base region (around 5.2 km) changed sharply along the different altitudes. This wind shear could induce turbulence
in this region, thereby establishing conditions conducive to disrupting the horizontal orientation of ice crystals.

Figure 7 shows the normalized frequency of HOIC and ROIC under different horizontal wind speed and temperature condi-
tions. It can be concluded that HOIC usually occurs accompanied by smaller horizontal wind speeds and higher temperatures.
Higher temperatures (-8 °C$> T > -22$ °C) favor the formation of plate-like ice crystals, while weaker horizontal winds exert
less torque to disturb their quasi-horizontal orientation. Additionally, Figure 7c shows the density scatter plot of horizontal
wind speed and temperature conditions where HOICs occur. High concentration (deep green) of HOIC bins lies at higher
temperatures (-5 °C to -18 °C) and lower horizontal wind speed (2 to 20 m s^{-1}). A negative correlation is found between
horizontal wind speed and temperature where HOICs exist. Overall, in the troposphere, higher altitudes are associated with
lower temperatures and stronger horizontal winds—a pattern that also applies to regions where HOICs are present. It should
be noted that the non-detection of HOICs at higher altitudes due to lidar signal attenuation may introduce a slight bias in the
results, potentially leading to an overestimation of temperature and an underestimation of horizontal wind speed. This limita-
tion is common in ground-based lidar studies of clouds. However, based on radar observations indicating a cloud top height of
approximately 7 km and radiosonde data showing a minimum temperature above -22°C and maximum horizontal wind speeds
below 25 m s^{-1}, the overall bias is expected to be minor. Therefore, the main conclusions of this study remain robust.

4.3 Cloud radar observations

From cloud radar observations, we can obtain reflectivity, Doppler velocity, and spectral width for HOICs and ROICs as shown
in Fig. 8. The Doppler velocity for HOICs is more narrow and shows a smaller maximum value than that for ROICs, which is
consistent with the findings by (Westbrook et al., 2010). The median Doppler velocity of HOIC is approximately -0.8 m s^{-1},
and as Westbrook et al. (2010) shows from their Doppler lidar observation, the fall speeds for the oriented ice are about
-0.3 m s^{-1}. The longer wavelength of operation of cloud radar, compared to lidar, likely results in the measurement of higher
Doppler velocities, as they are more sensitive to larger particles than lidar. Generally, larger particles tend to have higher fall
velocities.

Figure 8(b) shows that the largest eddy dissipation rate ($> 10^{-3}$ m^2 s^{-3}) occurs only with ROICs. Low EDR occurs with
both ROIC and HOIC, there are no significant differences between these two orientations. Fig. 8(c) shows that the largest
spectral width corresponds to the presence of ROICs. The same behavior is found for the EDR (Fig. 8b). Bimodal structures
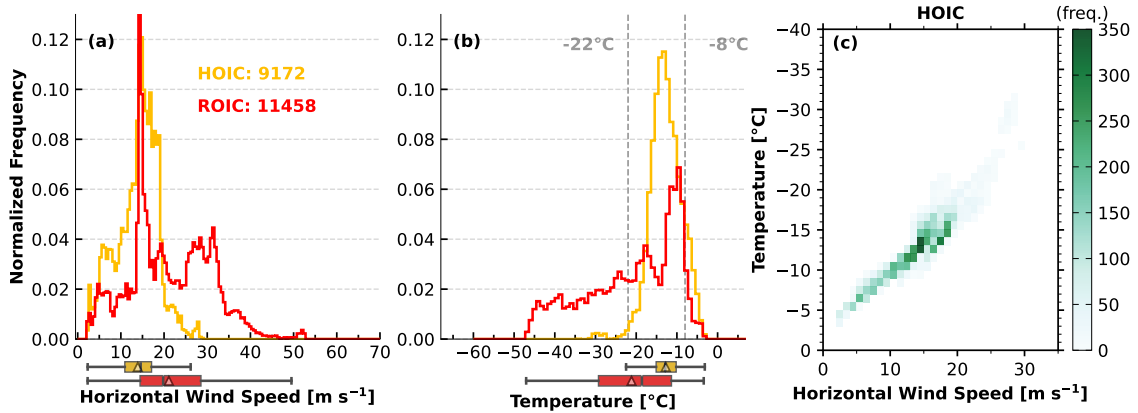are found for both EDR and spectral width.

Figure 7. Frequency distributions of environmental variables of different cloud phase classes on 13 October 2022. **(a)** The normalized histogram of the horizontal wind speed where HOICs and ROICs exist, with boxplots shown below the x-axis. The boxes extend from the lower to upper quartile values, with grey lines at the median, and triangles at the mean. The whiskers extend from the box to the minimum-maximum values or extend from the box by 1.5 times the interquartile range. The flyers are not shown in the plot. **(b)** The normalized histogram of temperature where HOICs and ROICs exist, with boxplots shown below the x-axis. **(c)** The density scatter plot of horizontal wind speed and temperature where HOICs exist, the greener the color, the higher the number density of HOIC bins.

The reflectivity shows larger values for HOICs than ROICs in this case. The peak of the HOICs (around -10 dBZ) is much higher than the peak of ROICs (around -20 dBZ), indicating that a larger nD^6 is detected in the bulk of the region where HOICs exist. Contrary to its sensitivity for the presence of columnar ice crystals (Li et al., 2021) or the melting layer (Li and Moisseev, 2020), the cloud radar LDR seems to be rather insensitive to HOIC as shown in Fig. 4(l). This is likely because the LDR of plate-like ice crystals is too small for the current sensitivity of cloud radar to detect.

4.4 Diameter and Reynolds number retrieved for HOICs

Figure 9 shows the diameter and Reynolds number of HOICs retrieved with an aerodynamic model by assuming that the shape of HOIC can be described by a hexagonal plate. The retrieval methods are described in Appendix D in detail. A summary of the statistical properties of estimated diameters and Reynolds numbers are listed in Table 1. The crystal diameters are mostly between 700 and 2000 µm, with a median of 1355 µm and a mean of 1367 µm, which is consistent with the values of 100–3000 µm from Polarization and Directionality of the Earth Reflectances (POLDER) data (Bréon and Dubrulle, 2004, Fig. 10). Sassen (1980) revealed that a crystal diameter of > 100–200 µm is needed for maintaining the horizontal orientation using photographic analyses of light pillar displays. He et al. (2021a) reported estimated diameters of 464–1305 µm for HOICs in 12 cases, with associated Reynolds numbers of 4–58 using a profile-based approach.

Most of the retrieved Reynolds numbers are between 1 and 100 (see Fig. 9d), which coincides with the value of 0.39–80 from the estimation based on spaceborne passive satellite observation (Bréon and Dubrulle, 2004). This study used a range-bin-based approach to obtain a wider range of Reynolds numbers than He et al. (2021a)'s falling profile-based approach. Kajikawa
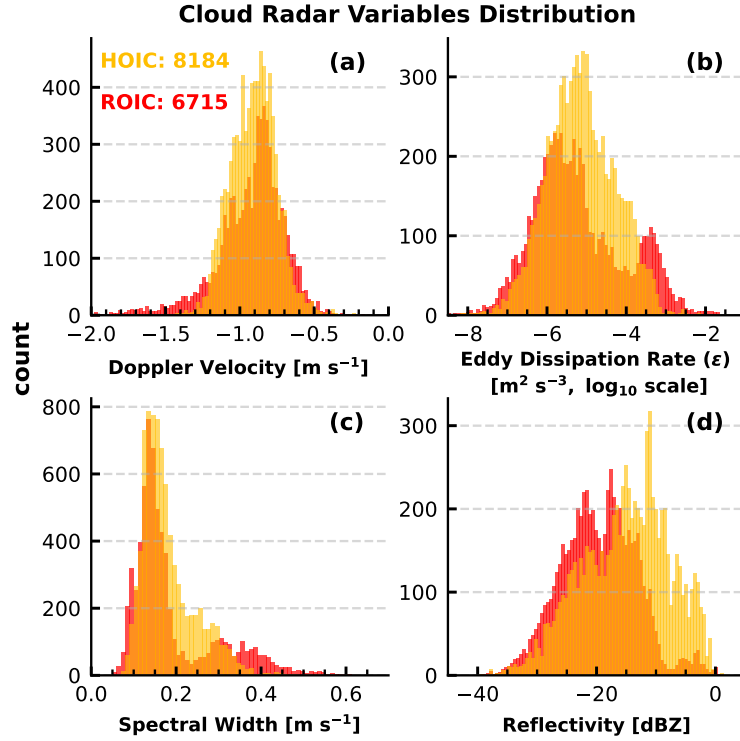
16

Figure 8. Cloud radar variables distributions of different cloud phases on 13 October 2022. Where HOICs and ROICs exist **(a)** the histogram of Doppler velocity. **(b)** the histogram of retrieved eddy dissipation rate. **(c)** the histogram of spectral width. **(d)** the histogram of reflectivity.

(1992) measured the lower critical values of the Reynolds number for unstable falling motion (random orientation) of ice
380   crystals, resulting in 47 to 90.7 based on the different crystal shapes (47 for hexagonal plate).

Table 1. Statistics of estimated diameter and Reynolds number for HOICs on 13 October 2022.

Statistics	Diameter [μm]	Reynolds number
5th percentile	1029	28
First quartile	1204	39
Median	1354	51
Third quartile	1525	65
95th percentile	1756	88
Mean	1369	54
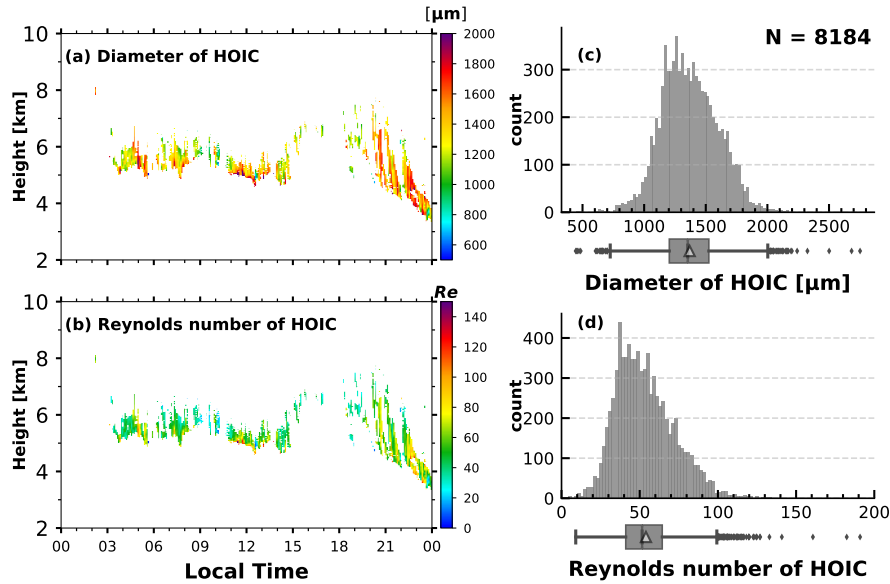
Figure 9. (a) Diameter and **(b)** Reynolds number of HOIC retrieved on 13 October 2022, time-height contour plots (5 min / 15 m resolution). And histogram of HOIC's retrieved diameter **(c)** and Reynolds number **(d)**, with the boxplots below the x-axis (the boxes extend from the lower to upper quartile values, with grey lines at the median, triangles at the mean. The whiskers extend from the box to the minimum-maximum values or extend from the box by 1.5 times the interquartile range).

4.5 Relationship between supercooled water cloud and HOICs

At heights above identified HOIC bins, we can sometimes find some supercooled water bins. As Westbrook et al. (2010) point out, supercooled water clouds likely play an important role in the formation of HOIC. Since we have a supercooled water cloud product (light blue in Fig. 4g and Fig.10), we can also prelimiarily investigate the relationship between the occurrence of the 385 supercooled water cloud class and HOICs based on the case study.

Especially at times after 16:00, Fig. 4 indicates the supercooled water on top of the identified HOIC regions, similar as was discussed earlier by, e.g., Westbrook et al. (2010) and He et al. (2021a). Probably the pristine ice crystals which are generated in the supercooled water layers are more liable to maintain a horizontal orientation. In turn, aging and further processing of ice crystals by means of riming, aggregation, or breakup probably alters the ice crystal structure toward more complex shapes 390 which are associated to a smaller torque and a corresponding lower attitude to maintain the orientation. At times before 16:00 in Fig. 4, the scenario is more complex. For this period, a comparison to the cloud radar observation (Fig. 4k) indicates that the signals of both lidar systems were subject to strong attenuation. For most of the time, the cloud radar detected much higher cloud tops as was identified by the lidars. This was especially the case for those time periods where HOIC was identified. It is thus likely that (1) the HOIC were formed at higher altitudes/lower temperatures and (2) that a relationship to the existence 395 of liquid water cannot be directly evaluated because no liquid layers could be identified due to the strong attenuation. Apart

18

from this caveat, the temperatures of the radar-derived cloud tops provide strong hints that liquid water was also involved in the formation of the HOIC observed before 16:00. As noted in Fig. 4k, the top temperatures were generally above $-25\,°C$. It is known from previous studies (De Boer et al., 2011; Westbrook and Illingworth, 2011) that ice forms only via the liquid phase at temperatures above that threshold. It should be noted that the scattering volume of lidars and radar is not exactly the same.

400   Small liquid droplets and optically thin ice clouds are sometimes not detectable from Ka-band radar compared with lidars.

Taking the above discussed indications granted, it appears reasonable to evaluate the relationship between the occurrence of liquid water and HOIC in more detail in a quantitative way. While this attempt is promising based on case studies of well-defined scenarios, such as for ice formation in stratiform supercooled liquid clouds, a statistically comprehensive approach that covers the full variety of cloud types is challenging. One reason is that often the lidar signal is attenuated already within the ice

405   virgae below, so that no signatures of liquid-dominated ice forming layers can be observed. Cloud radar techniques, in turn, are frequently not sensitive enough to detect layers of liquid water. Second reason is, that the ice-forming supercooled liquid water layers might eventually disappear due to cloud dynamical or microphysical processes, while the formed ice particles still exist. A third reason is that vertical wind shear and the microphysical evolution of the ice particles during falling blur the signatures of potential direct relationships between liquid layers and HOIC occurrence.

410   In here, we introduce the application of the Euclidean distance between supercooled liquid water bins and HOIC or ROIC, respectively, as an approach to quantify the impact of supercooled liquid water on HOIC formation. The relationship which was derived for the observations on 13 October 2022 is shown in Fig. 10. The Euclidean distance is derived by taking the square root of the sum of the squares of the horizontal and vertical distances. The horizontal distance was computed by multiplying the horizontal wind component from ERA5 by the time interval between the bins, while the vertical distance is the height

415   difference between the targeted bins. Moreover, considering the inherent falling characteristics of ice crystals and the general increase of the wind velocity with height, we focus solely on the earlier (leftward in the time-height cross-section) and higher (upward in the time-height cross-section) supercooled water cloud bins, as they potentially affect the alignment of the ice crystals. From Fig. 10a it can be seen that HOICs in comparison to ROICs are in general closer (brighter in color shade) to regions of supercooled liquid water.

420   Figure 10b illustrates the quantitative statistical analysis of the Euclidean distance between HOICs and supercooled water bins. From this Figure, it is evident that the Euclidean distance for HOICs relative to bins of supercooled liquid water is smaller than that for ROICs, with both a lower median and mean value. This indicates that HOICs are, in general, physically closer to supercooled water clouds. Even considering potential lidar attenuation in this instance, it is still possible to preliminarily conclude that supercooled water droplets may play a significant role in the formation of orientation. It is plausible that pristine

425   ice crystals, generated at cloud top temperatures between -8 °C and -22 °C, are more likely to induce horizontal orientation with large facets to counteract drag force. Future research should encompass more extensive studies on this subject.
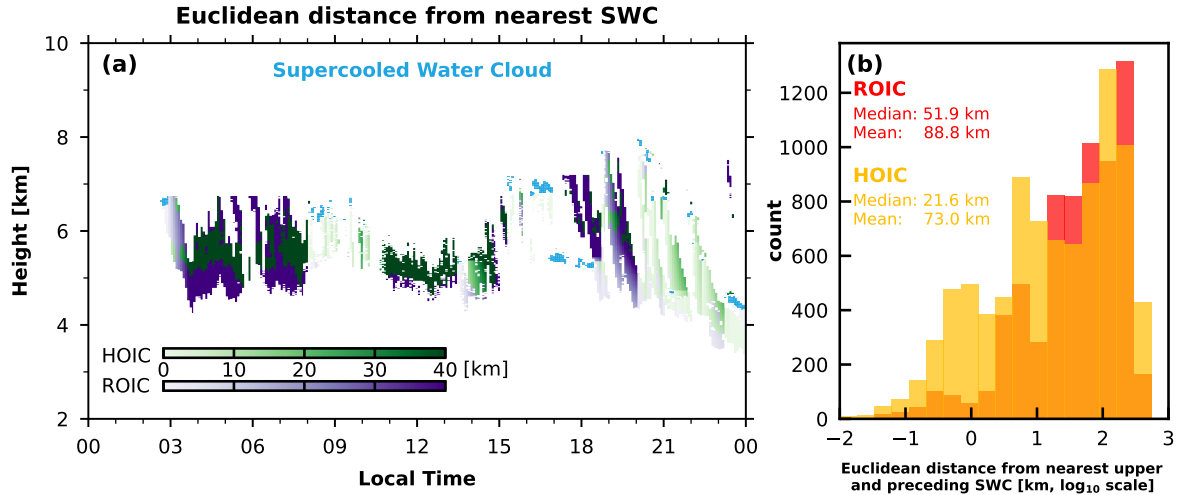
Figure 10. (a) The time-height cross-section of the Euclidean distance between the HOICs, ROICs, and supercooled water cloud bins on 13 Oct. 2022. The light blue range bins represent the supercooled water cloud bins. The color indicates the Euclidean distance; the darker the color (dark green and dark purple), the farther the Euclidean distance. Note here we use a green colorbar instead of orange for HOICs and a purple colorbar instead of red for ROICs to better discriminate HOIC and ROIC with different lightness of color. **(b)** The histogram of the Euclidean distance between the HOICs, ROICs, and supercooled water cloud bins on 13 Oct. 2022 in $\log_{10}$ scale with the median and mean value noted in the upper left corner.

5   Summary and conclusions

In this study, we developed a novel range-resolved detection method for horizontally oriented ice crystals (HOICs) using a combination of zenith-pointing and 15-degree off-zenith-pointing polarization lidars, in Beijing, China. In synergy with collocated observations from cloud radar, radiosonde data, and the ERA5 dataset, our approach provides unprecedented detail in HOIC detection and characterization of HOICs. This enhancement facilitates improvements in both the spatial and temporal resolution of these observations, thereby enabling a comprehensive investigation into the phenomenological aspects of HOIC events. One of the key findings of this research is the enhanced turbulence eddy dissipation rates (EDR) observed near the cloud base, which corresponds to the "switch-off" phenomenon of horizontal orientation in ice crystals. We attribute this phenomenon to the latent heat released from ice crystal sublimation. This discovery represents a significant advancement over previous studies, providing new insights into the role of turbulence in disrupting the horizontal alignment of ice crystals.

Our case study showed that HOICs form in relatively warm temperatures ($-8\,°C$ to $-22\,°C$) where plate-like ice crystals exist and the presence of rather light wind speeds ($0–20\,\mathrm{m\,s^{-1}}$). Cloud radar indicates that mean Doppler velocity is similar for HOICs and ROICs (randomly oriented ice crystals), but more concentrated for HOICs. The highest EDR and spectral width are exclusive to ROICs, while HOICs generally have larger reflectivity. Moreover, the estimated diameter using Doppler cloud radar and the aerodynamic model (ranging from approximately 1029 μm to 1756 μm for 5th and 95th percentiles) and

Reynolds numbers (28 to 88 for 5th and 95th percentiles) provide a clearer understanding of HOICs' microphysical properties. Moreover, our observations suggest a strong relationship between supercooled water clouds and HOIC formation, with a closer Euclidean distance between supercooled water cloud bins for HOICs than ROICs. The HOIC persisted for nearly the whole day in this case, indicating the HOIC could significantly impact the radiation balance. These findings could help improve the parameterization schemes in climate models, especially in mid-latitude regions like Beijing.

In this paper, we only show one typical case to demonstrate the HOIC identification method. More case studies could be shown in the following work to show different conditions for HOICs (different cloud top temperatures). The observation method and detection algorithm developed in this research provide new tools for long-term HOIC observation, due to the precise range bin identification of HOICs and continuous observation, future work of diurnal and seasonal characteristics will be established through the yearlong dataset. Since this dataset enables the joint classification of both supercooled water cloud bins and HOIC, it provides a unique dataset to investigate the relationship between supercooled water and HOIC, which could shed light on the generation mechanism of HOICs, as previously revealed by Westbrook et al. (2010) and the Euclidean-distance approach presented within our study. We see a high potential in using the Euclidean distance approach, even though an improved quantification will require an enhanced characterization of the presence of liquid water beyond lidar attenuation (e.g., Schimmel et al., 2022) and an improved consideration of the ice crystal evolution during sedimentation (Vogl et al., 2024). Except for the relationship between supercooled water and HOIC, even recent studies suggest HOICs are often correlated in precipitating clouds and their ice nucleation processes have a connection with precipitation formation (Ross et al., 2017; Kikuchi and Suzuki, 2019). In addition, the orientation of ice crystals is always a mixture in a bulk volume, and the horizontal orientation is kind of quasi-horizontally oriented, with some flutter or wobbling angles. The fraction of HOIC inside a range bin and the flutter angle could be retrieved with the help of HOICs model data (Borovoi et al., 2018; Saito and Yang, 2019). Further studies are required to help derive the ratio of HOIC/ROIC. What's more, in this study, we only use two elastic lidars, long-term Raman lidars and HSRLs observation could be employed to accurately determine the lidar ratio and particle depolarization ratio to provide more information about HOICs in the future.

Like all the lidar-based research, lidar attenuation for opaque clouds (i.e. optical depths roughly above 3) is a main defect for this method, so some upmost cloud range bins are missed. With cloud radar, we can infer the cloud top beyond lidar attenuation to a certain extent. Future ice crystal orientation detection work based on radar should be carried out to make up for this defect (Hajipour et al., 2024). The assumption of pure hexagonal plates in the diameter and Reynolds number retrieval is the simplest, highly symmetrical crystal. In practice, many other planar crystals exist. Using Doppler velocity to estimate the ice crystal diameter is a rough estimation because the superposition of air movement is ignored. Future retrieval could consider deriving the ice crystal size utilizing the ratio of radar reflectivity and the lidar extinction (Bühl et al., 2019; Ansmann et al., 2024). So some uncertainty could exist in the estimation of diameter and Reynolds number process. We only consider the middle part of the retrieved data, without the extreme value. In conclusion, we find the collection of retrieval techniques and approaches for HOIC classification and characterization, that was presented in this study, a valuable toolset for statistical evaluations that cover larger time periods. This possibility is granted by means of the 1-year dataset from Beijing that was introduced only

briefly here. In a follow-up study, a statistical evaluation of the relationship between HOIC and other cloud microphysical and environmental parameters will be presented.

Appendix A: AVORS lidar optomechanical setup

Figure A1 is the optomechanical setup of the AVORS lidar, an image courtesy of AVORS Technology. Note two photomultiplier tubes (PMT, Model Hamamatsu H10682-210) are used in the system.
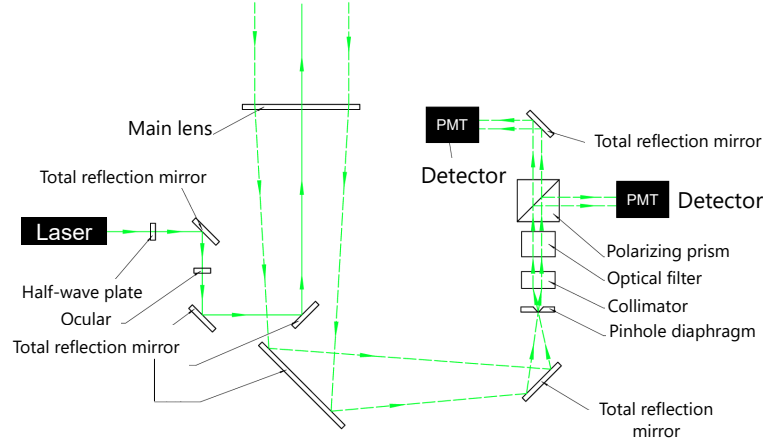

Figure A1. Schematic of the AVORS lidar optomechanical setup

Appendix B: Lidar calibration

B1 Lidar system constant calibration

This step is from the lidar's original photon count number to lidar attenuated backscatter, to make the zenith-pointing and off-zenith pointing lidars' backscatter signal comparable. First, for the MPL and AVORS lidar, both two lidars use a photon count system. The photo count rate times dead time correction then minus the afterpulse value for MPL (no need for afterpulse for AVORS lidar after the manufacturer's test), then minus the background, times the square of range and divided by overlap function and laser energy. The above steps are summarize as the Eqs. B1 and B2:

$$\text{NRB}_{\text{MPL}} = \frac{[(Photo\ Count\ Rate \times Dead\ Time\ Correction) - Afterpulse - Background] \times range^2}{Overlap \times Laser\ Energy} \tag{B1}$$

$$\text{NRB}_{\text{AVORS}} = \frac{[(Photo\ Count\ Rate \times Dead\ Time\ Correction) - Background] \times range^2}{Overlap \times Laser\ Energy} \tag{B2}$$

Table A1. Specifications of the Portable Particle Lidar by AVORS Technology

Specifications	Value
Transmitter	
Laser wavelength (nm)	532
Laser energy (μJ)	20
Pulse width (ns)	≤ 10
Emission laser pulse linewidth (nm)	≤ 0.2
Linear polarization purity	> 100:1
Divergence angle (mrad)	< 1
Receiver	
Diameter of narrow-FOV telescope (mm)	160
FOV of narrow-FOV telescope (mrad)	< 0.2
Detector and DAQ	
Manufacturer of detector	Hamamatsu
Type of detector	PMT, H10682-210
Photodetector mode	Photon counting
Sampling rate of DAQ (MHz)	> 10
Sampling bits	Photon counting channel: 200 M c/s
Interference filter	Bandwidth: ≤ 0.2 nm
	Out-of-band suppression $\geq$ OD4

In this way, we get the normalized relative backscatter (NRB). Then we employ PollyNet's calibration method (Baars et al., 2016; Yin et al., 2020) to two lidars' NRB profiles. Namely first Rayleigh fit, i.e. find the aerosol-free region. Then we suppose a fixed lidar ratio of 50 sr, using the Klett-Fernald method to retrieve extinction profile (Fernald, 1984). After that, we integrate the extinction profiles to get the height-resolved aerosol optical depth (AOD) and the lidar calibration constant, then we employ a
495 smooth method to the lidar calibration constant profile to determine the final lidar calibration constant. After that, the attenuated backscatter can be derived by NRB divided by the lidar calibration constant.

B2 Lidar depolarization calibration

Lidar depolarization is the key feature that distinguishes the HOIC. HOIC shows a much lower depolarization ratio than ROIC for zenith-pointing lidar (He et al., 2021a). Before the identification of HOIC, we must confirm the reliability of our
500 lidars' depolarization ratio. Since the MPL and AVORS lidar are both compact, small-sized lidars, the standard $\Delta 90$ method

(Freudenthaler, 2016) is not applicable. We use the well-calibrated Raman lidar to get the depolarization ratio, and match the same time's MPL and AVORS lidar depolarization ratio.

Due to the MPL has only one detector for two polarization channels (Flynna et al., 2007), there is no gain ratio effect here (or gain ratio $K^* = 1$ in Papetta et al.'s case, see Eq. (B3)), we use the Córdoba-Jabonero et al. (2021) method to calibrate the MPL's depolarization, namely assuming a constant deviation compared with the reference Raman lidar. Figure B1a, b are the scatter plots between the MPL depolarization ratios and reference Raman lidar depolarization ratios on 5 March 2022 from 00:00 to 06:00 and 14 April 2022 from 00:00 to 05:00, respectively, showing a constant intercept of -0.020 ± 0.001. Additional cases (not shown here) from 00:00 to 01:00 on 26 February 2022 and from 00:00 to 05:00 on 7 May 2022 further validate the consistency of the -0.02 offset. Then we simply use $\delta_{\mathrm{MPLcalibrated}} = \delta_{\mathrm{MPL}} - 0.02$ to calibrate the MPL depolarization. Figure B1c, d show the calibrated MPL depolarization ratio profiles (purple) and the observed uncalibrated ones (orange), indicating well agreement of depolarization ratio between the calibrated MPL and the reference Raman lidar. Note as it shows in Fig. B1c, for calibrated MPL depolarization ratio profile, there is a slight difference left from Raman lidar (≈ 0.01) below 2.5 km, but it is still acceptable. From our observation, the region below 2 km, where this difference is most pronounced, is generally unimportant for identifying HOICs (in the 13 October 2022 case, HOICs are above 4 km). Therefore, the imperfect performance of the calibrated depolarization ratio in this layer has minimal impact on HOIC detection.

For AVORS lidar, since it has two detectors for each polarization channel (similar to the Cimel CE376 lidar system used in Papetta's case, see Fig. A1), we use the newly proposed Papetta's two-parameter method to calibrate the depolarization of the lidars (Papetta et al., 2024, Eq. (10)). The two parameters are K^*, the gain ratio between the two channels, and g, the cross-talk from the co-polar signal to the cross-polar signal.

Using δ^* to denote uncalibrated AVORS lidar depolarization ratio, or observed depolarization ratio, the calibrated AVORS lidar depolarization ratio (δ) can be expressed using K^* and g:

$$\delta = \frac{\delta^*}{K^*} - g \tag{B3}$$

Then we select one dust layer and one aerosol-free region as reference, we use the $\delta_{\mathrm{ref}}^{\mathrm{d}}$ from the reference Raman lidar observation and theoretical molecular depolarization δ_{m} 0.004 (Behrendt and Nakamura, 2002), and we select the observed lidar depolarization ratio of dust layer (δ_{d}^*) and the molecular layer (δ_{m}^*).

$$\delta_{\mathrm{ref}}^{\mathrm{d}} = \frac{\delta_{\mathrm{d}}^*}{K^*} - g \tag{B4}$$

$$\delta_{\mathrm{m}} = \frac{\delta_{\mathrm{m}}^*}{K^*} - g \tag{B5}$$

With two unknowns and two equations, the K^* and g could be solved using:

$$K^* = \frac{\delta_{\mathrm{d}}^* - \delta_{\mathrm{m}}^*}{\delta_{\mathrm{ref}}^{\mathrm{d}} - \delta_{\mathrm{m}}} \tag{B6}$$

$$g = \frac{\delta_{\mathrm{m}}^* \delta_{\mathrm{ref}}^{\mathrm{d}} - \delta_{\mathrm{d}}^* \delta_{\mathrm{m}}}{\delta_{\mathrm{d}}^* - \delta_{\mathrm{m}}^*} \tag{B7}$$

What's more, Fig. B1c shows the case (5 March 2022, 00:00-06:00) used for AVORS lidar depolarization calibration. Similar to Papetta's case, we select the molecule region around 7-7.5 km (Eq. (B5)) and dust region around 1 km (Eq. (B4)) as reference, both region was denoted with grey frame in Fig. 2c. After that we can get $K^* = 0.954$ and $g = 0.0329$ from Eqs. (B6) and (B7). Three additional cases—00:00–01:00 on February 26, 2022; 00:00–05:00 on April 14, 2022; and 00:00–05:00 on May 7, 2022—were selected using a consistent method involving molecule and dust regions to derive robust K^* and g values. The resulting K^* and g values are presented in Fig. B3 with statistics. Ultimately, we obtained $K^* = 0.962 \pm 0.006$ and $g = 0.0327 \pm 0.0009$. The calibrated depolarization ratio profile was calculated from Eq. (B3) using the robust K^* and g. Figure B1c shows the calibrated AVORS lidar depolarization (black) and the observed one (pink). We can find that after calibration, the AVORS lidar depolarization ratio is very close to the reference Raman lidar (see Fig. B1c, back line, and blue line).

Figure B1d shows the calibrated MPL and AVORS lidar and the Raman lidar depolarization ratio profiles on 14 April 2022 from 00:00 to 05:00 (another case). For the molecule (above 11 km) and dust region (below 4km), the three lidars' depolarization ratio profiles match perfectly, indicating the calibration method used here for two lidars shows good performance. For the cirrus region between 7.5 km and 11 km, however, there is a slight difference between the three lidars' depolarization ratio, which could be explained by the three lidars having different fields of view (Raman 2.3 mrad, MPL 0.1 mrad, AVORS 0.2 mrad), multiple scattering effects with the cloud could contribute some uncertainty. And since the AVORS lidar was off-zenith pointing (Raman lidar and MPL are both zenith-pointing), maybe some horizontal heterogeneity of the cirrus exists. Nevertheless, the slight difference is affordable for our algorithm Fig. 2 to distinguish HOIC. Sensitivity tests were performed to evaluate the stability of the 0.6 threshold (ratio of zenith to off-zenith depolarization) used in the classification flowchart (Fig. 2). Assuming typical depolarization uncertainties (5–10%, percentual error) as shown in Fig. B1, the analysis based on long-term statistics of ice-containing clouds indicates that the percentage of falsely identified HOICs and ROICs below 2-5%, which corroborates the tolerance of the classification scheme to uncertainties in the depolarization. Note the Raman lidar depolarization matches very well with theoretical molecular depolarization 0.004 (Fig. B1c, d above 7 km and 11km, respectively), showing excellent depolarization performance as a reference lidar.

There is a period (from 9 May 2023 to 3 June 2023) when both MPL and AVORS lidar were zenith-pointing, we can utilize this period to validate our depolarization calibration result. Figure B2 shows the density scatter plot of MPL and AVORS lidar calibrated depolarization ratio of the cloud, aerosol, and molecule range bins observed during both lidar's zenith-pointing period. The least-square squares fitting line (green dashed line) nearly overlaps with the 1:1 line (black dashed line), indicating well agreement of two lidars depolarization after calibration. According to the methods described above, we use the calibrated depolarization of MPL an AVORS lidar for the categorization algorithm and other analysis in this study.
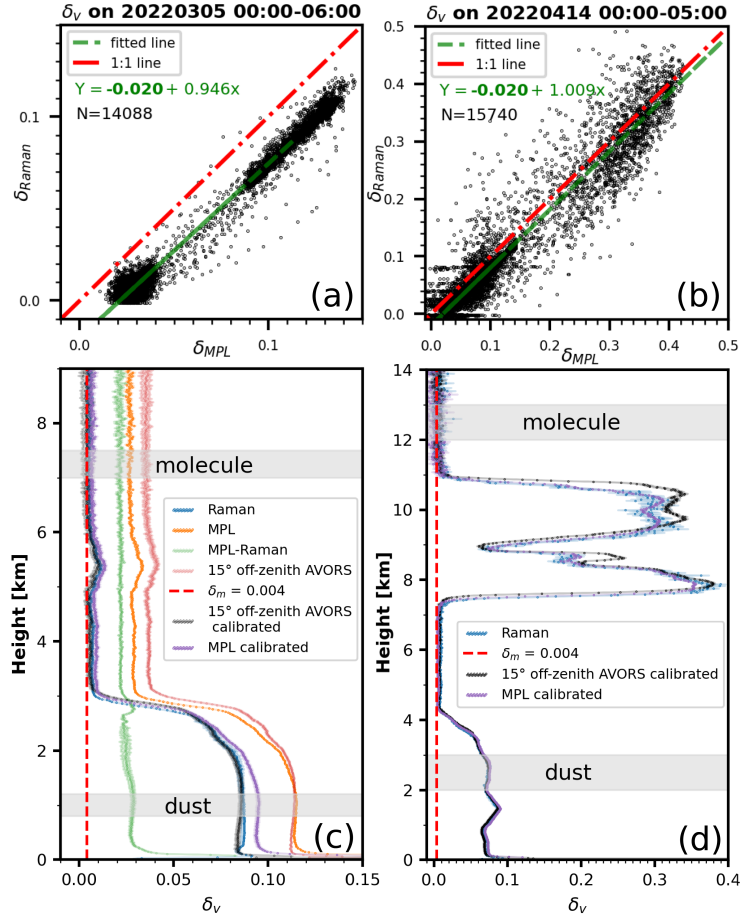
Figure B1. Scatter plot of well-calibrated Raman lidar and MPL uncalibrated depolarization ratio on (a) 5 March 2022, 00:00-06:00, Local Time and (b) 14 April 2022, 00:00-05:00, Local Time; (c) Averaged Depolarization profiles on 5 March 2022, 0:00-06:00; (d) Averaged Depolarization profiles on 14 April 2022, 00:00-05:00; The horizontal gray shaded areas indicate the reference ranges used for dust and molecular layers. The shaded regions around the lines represent the uncertainties associated with depolarization ratio calculation and calibration.

Appendix C: Description of RH calculation

The vapor pressure E could be calculated from the following equation:

$$E = \frac{rP}{0.622 + r} \tag{C1}$$

Where r is the water vapor mixing ratio. Here we use the specific humidity (q) from ERA 5 data ($r = \frac{q}{1-q}$, since $q \ll 1$, $r \approx q$).

The saturated water vapor pressure with respect to liquid water E_w and ice E_i can be calculated from the following empirical formulas (Murray, 1967; Bolton, 1980):

26
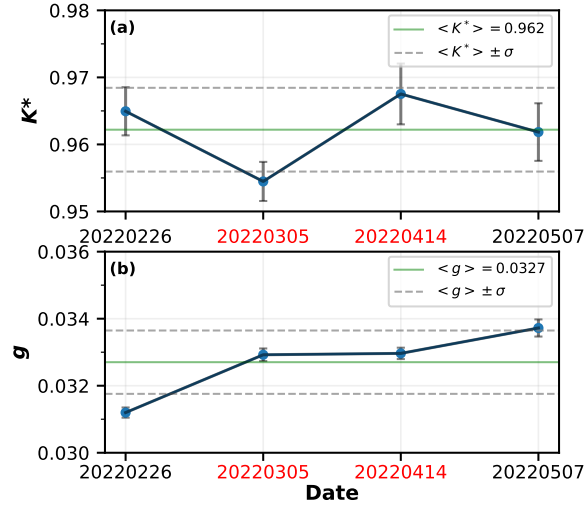
Figure B2. Temporal evolution of polarization parameters derived using the two-parameter approach. Error bars indicate the variability of the derived parameters within the selected molecular scattering and dust reference layers. The average polarization parameter value and its standard deviation in the whole period is shown by solid green lines and dashed gray lines, respectively. The timestamps of the cases shown in Fig. B1 are highlighted in red.
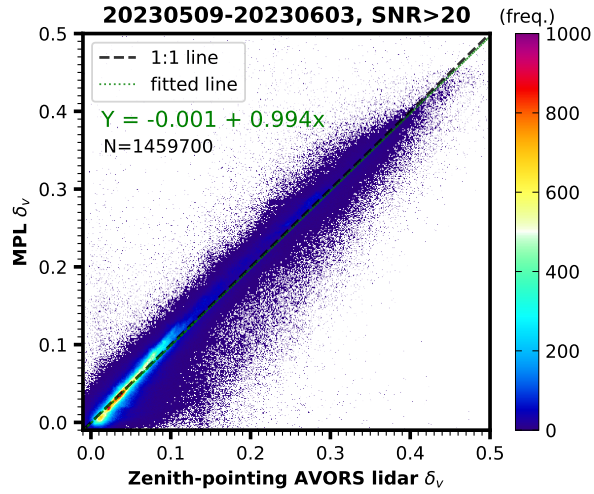

Figure B3. The density scatter plot between the zenith-pointing AVORS lidar and the MPL-calibrated depolarization ratio from 9 May 2023 to 3 June 2023, when two lidars are both zenith-pointing. Points including clouds, aerosols, and molecules with signal-to-noise ratios greater than 20 are used to plot the figure.

$$E_\mathrm{w} = 6.112 \exp\left[\frac{17.67(T - 273.16)}{T - 29.65}\right] \tag{C2}$$

$$E_i = 6.1078\exp\left[\frac{21.87(T-273.16)}{T-7.66}\right] \tag{C3}$$

where T is the temperature provided by radiosonde or ERA5. Then, relative humidity over water ($\mathrm{RH_w}$) and ice ($\mathrm{RH_i}$) could be calculated by

$$\mathrm{RH_w} = \frac{E}{E_w} \tag{C4}$$

575

$$\mathrm{RH_i} = \frac{E}{E_i} = \frac{\mathrm{RH_w}E_w}{E_i} \tag{C5}$$

For radiosonde, $\mathrm{RH_w}$ is provided, we use Eqs. (C2), (C3), and (C5) to get the $\mathrm{RH_i}$ profile. For ERA5 $\mathrm{RH_i}$ data, however, due to the ERA5 relative humidity is a piecewise function of saturation over water and ice (> 0°C over water, < -23°C over ice, between -23°C and 0°C interpolating the value over ice and water). We use the specific humidity to calculate the $\mathrm{RH_i}$ and $\mathrm{RH_w}$ separately (Eqs. (C1) to (C5)).

Appendix D: Reynolds number and diameter calculation for falling ice crystals

The diameter and Reynolds number of horizontally oriented ice crystals can be estimated from the terminal falling velocity measured by Doppler cloud radar for further discussion (He et al., 2021a). Here we use the approach proposed by Heymsfield and Westbrook (2010). First, as the columns have a negligible impact on specular reflection compared to the plates (Zhou et al., 2012a), which present significantly larger surfaces to the incident lidar beam, we assume the HOIC shape is hexagonal plate and the thickness $h = 0.04D$, where D is the diameter of ice crystal (Beard, 1980). The mass of a single ice crystal is then $m = \frac{3\sqrt{3}}{8}D^2 \times h \times \rho_{ice}$. The area ratio of ice crystal A_r is define as $A_r = A/[(\pi/4)D^2]$. For horizontally oriented hexagonal plate ice crystal, $A_r = 0.827$.

The corresponding modified Davies number is defined as:

$$X = \frac{\rho_{air}}{\eta^2}\frac{8mg}{\pi A_r^{1-k}} \tag{D1}$$

where the optimum value of k is 0.5. The density of air ρ_{air} is the function of pressure (P) and temperature (T), and can be calculated by:

$$\rho_{air} = 1.293 \times \frac{P}{P_0} \times \frac{273.15}{T} \tag{D2}$$

where $P_0 = 1013.25$ hPa is the standard atmospheric pressure, P and T are interpolated from ERA5 data.

Air dynamic viscosity η is defined as:

$$\eta = \eta_0 \times (\frac{T}{288.15})^{1.5} \times \frac{288.15+B}{T+B} \tag{D3}$$

where η_0 is the air dynamic viscosity at 15 °C, $\eta_0 = 1.7894 \times 10^{-5}$ Pa· s (T = 15°C) and B is a gas-type-related constant, $B = 110.4$ K.

The Reynolds number Re can be expressed as a function of Davies number:

$$Re = \frac{\delta_0^2}{4}\left[\left(1 + \frac{4\sqrt{X}}{\delta_0^2\sqrt{C_0}}\right)^{1/2} - 1\right] \tag{D4}$$

where the inviscid coefficient $C_0 = 0.35$ and the dimensionless coefficient $\delta_0 = 8.0$. Finally, the crystal diameter D can be calculated through the following equation:

$$D = \frac{\eta Re}{\rho_{air} v_t} \tag{D5}$$

where v_t is estimated by cloud radar Doppler velocity.

Finally, from Eqs. (D1), (D4), and (D5), we can retrieve the diameter of the horizontally oriented ice crystal and the corresponding Reynolds number. After conducting careful sensitivity tests, we found that the assumed fixed aspect ratio (h/D) of 0.04 yields a retrieved diameter and Reynolds number similar to those obtained using empirical dynamic aspect ratio relationships reported in the literature (Bréon and Dubrulle, 2004; Saito and Yang, 2019). It is important to note that crystal diameter and Reynolds number are highly sensitive to the shape of ice crystals (Westbrook et al., 2010, Table III). The assumed HOIC shape of hexagonal plates is the most simplified and widely used model (Bréon and Dubrulle, 2004; Zhou et al., 2012b; He et al., 2021a). Additionally, assuming that Doppler velocity represents the terminal velocity of a particle in still air introduces some uncertainty. However, in general, long-term Doppler velocity measurements can partially mitigate the effect of rapidly changing vertical airflow and provide an approximate still-air velocity for falling ice crystals. To reduce the potential uncertainty caused by extreme vertical airflow, we focus only on the intermediate range of the retrieved diameters and Reynolds numbers, excluding extreme values (e.g., data points beyond the 5th and 95th percentiles). In summary, this method serves as an estimation to compare the case with previous studies (Westbrook et al., 2010; He et al., 2021a).

Appendix E: Calculation of eddy dissipation rates

The turbulence eddy dissipation rate (or turbulent kinetic energy dissipation rate, EDR, ϵ) is a measure of the rate at which turbulent kinetic energy is converted into thermal energy due to viscous dissipation in a fluid. It quantifies how energy from larger turbulent eddies is transferred to smaller eddies and ultimately dissipated as heat, indicating the intensity of turbulence. The turbulence eddy dissipation rate was computed to reflect the turbulence using quantities including the standard deviation of Doppler velocity and horizontal wind speed in this study (Bouniol et al., 2003; O'Connor et al., 2010).

The standard deviation of the average wind serves as a measure of the kinetic energy present in turbulent scales that are typically larger than the size of the sampled volume. ϵ can be inferred from the variability in the vertical velocity over the 300 s sample time, $\sigma_{\bar{v}}$ in Eq.(E1) is the standard deviation of Doppler velocity within 300 s for 13 s unit time. By integrating the

Kolmogorov (1941) turbulent energy spectrum formula within the inertial subrange, we can get:

$$\epsilon = \left(\frac{2}{3a}\right)^{3/2} \frac{\sigma_{\overline{v}}^3}{\left(k^{-2/3} - k_1^{-2/3}\right)^{3/2}} \tag{E1}$$

where $a = 0.55$ is one dimension Kolmogorov constant (Borque et al., 2016). And the wave number related to the large eddies traveling through the sampling volume during the sampling time is:

$$k = \frac{2\pi}{x_b + T_s|V_h|} \tag{E2}$$

where the width of the radar beam at height z is $x_b = 2z\sin(\theta/2)$ with $\theta = 0.35°$ for this cloud radar. $|V_h|$ is the modulus of the horizontal wind, interpolated from ERA5 data. T_s is the sampling time, 300 s in this case. And the wave number corresponding to the length scale describing the scattering volume dimension for the dwell time for a single sample is given by:

$$k_1 = \frac{2\pi}{x_b + t|V_h|} \tag{E3}$$

Where dwell time $t = 13$ s for this cloud radar's case. In this way, the turbulence eddy dissipation rate was estimated from Eqs. (E1), (E2), and (E3). Note Bouniol et al. (2003) uses the time period of 30 s for $\sigma_{\overline{v}}$ compute and shows the estimated EDR are not sensitive to the number of points used. And a recent study (Nijhuis et al., 2019) points out that 10 min is still within the inertial sub-range, so we use the 300 s (5 min) time interval to calculate standard deviation considering the consistency with other quantities' time resolution in this study.

Appendix F: List of abbreviations and symbols

Table F1. List of abbreviations (acronyms), symbols and their explanations

CALIPSO	Cloud-Aerosol Lidar and Infrared Pathfinder Satellite Observations
CALIOP	Cloud-Aerosol Lidar with Orthogonal Polarization
DSCOVR	Deep Space Climate Observatory
EDR	eddy dissipation rate
ECMWF	European Centre for Medium-Range Weather Forecast
EPIC	Earth Polychromatic Imaging Camera
ERA5	ECMWF Reanalysis v5
EarthCARE	Earth Cloud Aerosol and Radiation Explorer
HOIC	horizontally oriented ice crystal
LDR	linear depolarization ratio
MMCR	Millimeter-wave cloud radar
MPL	micro pulse lidar
MPC	mixed-phased cloud
NRB	normalized relative backscatter
PKU	Peking University
PMT	photomultiplier tube
POLDER	Polarization and Directionality of the Earth Reflectance
RH	relative humidity
ROIC	randomly oriented ice crystal
SNR	signal-to-noise ratio
SWC	supercooled water cloud
TKE	turbulent kinetic energy
β'	attenuated backscatter
β'_{zenith}	attenuated backscatter of zenith-pointing lidar
$\beta'_{\text{off-zenith}}$	attenuated backscatter of off-zenith-pointing lidar
$\delta_v(\delta)$	volume depolarization ratio
δ_{zenith}	volume depolarization ratio of zenith-pointing lidar
$\delta_{\text{off-zenith}}$	volume depolarization ratio of off-zenith-pointing lidar

References

Ansmann, A., Tesche, M., Althausen, D., Müller, D., Seifert, P., Freudenthaler, V., Heese, B., Wiegner, M., Pisani, G., Knippertz, P., et al.: Influence of Saharan dust on cloud glaciation in southern Morocco during the Saharan Mineral Dust Experiment, Journal of Geophysical Research: Atmospheres, 113, https://doi.org/10.1029/2007JD008785, 2008.

Ansmann, A., Jimenez, C., Knopf, D. A., Roschke, J., Bühl, J., Ohneiser, K., and Engelmann, R.: Impact of wildfire smoke on Arctic cirrus formation, part 2: simulation of MOSAiC 2019- 2020 cases, EGUsphere, 2024, 1–29, https://doi.org/10.5194/egusphere-2024-2009, 2024.

Baars, H., Kanitz, T., Engelmann, R., Althausen, D., Heese, B., Komppula, M., Preißler, J., Tesche, M., Ansmann, A., Wandinger, U., et al.: An overview of the first decade of Polly NET: an emerging network of automated Raman-polarization lidars for continuous aerosol profiling, Atmospheric Chemistry and Physics, 16, 5111–5137, https://doi.org/10.5194/acp-16-5111-2016, 2016.

Baars, H., Seifert, P., Engelmann, R., and Wandinger, U.: Target categorization of aerosol and clouds by continuous multiwavelength-polarization lidar measurements, Atmospheric Measurement Techniques, 10, 3175–3201, https://doi.org/10.5194/amt-10-3175-2017, 2017.

Bailey, M. P. and Hallett, J.: A comprehensive habit diagram for atmospheric ice crystals: Confirmation from the laboratory, AIRS II, and other field studies, Journal of the Atmospheric Sciences, 66, 2888–2899, https://doi.org/10.1175/2009JAS2883.1, 2009.

Beard, K.: The effects of altitude and electrical force on the terminal velocity of hydrometeors, Journal of Atmospheric Sciences, 37, 1363–1374, https://doi.org/10.1175/1520-0469(1980)037%3C1363:TEOAAE%3E2.0.CO;2, 1980.

Behrendt, A. and Nakamura, T.: Calculation of the calibration constant of polarization lidar and its dependency on atmospheric temperature, Optics express, 10, 805–817, https://doi.org/https://doi.org/10.1364/oe.10.000805, 2002.

Bian, Y., Liu, L., Zheng, J., Wu, S., and Dai, G.: Classification of cloud phase using combined ground-based polarization LiDAR and millimeter cloud radar observations over the Tibetan Plateau, IEEE Transactions on Geoscience and Remote Sensing, 61, 1–13, https://doi.org/10.1109/TGRS.2023.3313798, 2023.

Bolton, D.: The computation of equivalent potential temperature, Monthly weather review, 108, 1046–1053, https://doi.org/10.1175/1520-0493(1980)108%3C1046:TCOEPT%3E2.0.CO;2, 1980.

Borovoi, A., Reichardt, J., Görsdorf, U., Wolf, V., Konoshonkin, A., Shishko, V., and Kustova, N.: Retrieving microphysics of cirrus clouds from data measured with raman lidar ramses and a tilted ceilometer, in: EPJ Web of Conferences, vol. 176, p. 08002, EDP Sciences, https://doi.org/10.1051/epjconf/201817608002, 2018.

Borque, P., Luke, E., and Kollias, P.: On the unified estimation of turbulence eddy dissipation rate using Doppler cloud radars and lidars, Journal of Geophysical Research: Atmospheres, 121, 5972–5989, https://doi.org/10.1002/2015JD024543, 2016.

Bouniol, D., Illingworth, A., and Hogan, R.: Deriving turbulent kinetic energy dissipation rate within clouds using ground based radar, in: Proceedings of the European Conference on Radar in Meteorology and Hydrology, vol. 281, ERAD Publishing, Seattle, USA, https://copernicus.org/erad/2004/online/ERAD04_P_281.pdf, 2003.

Bréon, F.-M. and Dubrulle, B.: Horizontally oriented plates in clouds, Journal of the atmospheric sciences, 61, 2888–2898, https://doi.org/10.1175/JAS-3309.1, 2004.

Bühl, J., Seifert, P., Radenz, M., Baars, H., and Ansmann, A.: Ice crystal number concentration from lidar, cloud radar and radar wind profiler measurements, Atmospheric Measurement Techniques, 12, 6601–6617, https://doi.org/10.5194/amt-12-6601-2019, 2019.

Cairo, F., Di Donfrancesco, G., Adriani, A., Pulvirenti, L., and Fierli, F.: Comparison of various linear depolarization parameters measured by lidar, Applied Optics, 38, 4425–4432, https://doi.org/10.1364/AO.38.004425, 1999.

Chang, L., Li, J., Chu, Y., Dong, Y., Tan, W., Xu, X., Ren, J., Tian, X., Li, C., Liu, Z., et al.: Variability of surface aerosol properties at an urban site in Beijing based on two years of in-situ measurements, Atmospheric Research, 256, 105 562, https://doi.org/10.1016/j.atmosres.2021.105562, 2021.

700 Chu, Y., Li, J., Li, C., Tan, W., Su, T., and Li, J.: Seasonal and diurnal variability of planetary boundary layer height in Beijing: Intercomparison between MPL and WRF results, Atmospheric Research, 227, 1–13, https://doi.org/10.1016/J.ATMOSRES.2019.04.017, 2019.

Córdoba-Jabonero, C., Ansmann, A., Jiménez, C., Baars, H., López-Cayuela, M.-Á., and Engelmann, R.: Experimental assessment of a micro-pulse lidar system in comparison with reference lidar measurements for aerosol optical properties retrieval, Atmospheric Measurement Techniques, 14, 5225–5239, https://doi.org/10.5194/amt-14-5225-2021, 2021.

705 Dai, G., Wu, S., Long, W., Liu, J., Xie, Y., Sun, K., Meng, F., Song, X., Huang, Z., and Chen, W.: Aerosol and cloud data processing and optical property retrieval algorithms for the spaceborne ACDL/DQ-1, Atmospheric Measurement Techniques, 17, 1879–1890, https://doi.org/10.5194/amt-17-1879-2024, 2024.

De Boer, G., Morrison, H., Shupe, M., and Hildner, R.: Evidence of liquid dependent ice nucleation in high-latitude stratiform clouds from surface remote sensors, Geophysical Research Letters, 38, https://doi.org/10.1029/2010GL046016, 2011.

710 Ding, H., Li, H., and Liu, L.: Improved spectral processing for a multi-mode pulse compression Ka–Ku-band cloud radar system, Atmospheric Measurement Techniques, 15, 6181–6200, https://doi.org/10.5194/amt-15-6181-2022, 2022.

Engelmann, R., Kanitz, T., Baars, H., Heese, B., Althausen, D., Skupin, A., Wandinger, U., Komppula, M., Stachlewska, I. S., Amiridis, V., et al.: The automated multiwavelength Raman polarization and water-vapor lidar Polly XT: The neXT generation, Atmospheric Measurement Techniques, 9, 1767–1784, https://doi.org/10.5194/amt-9-1767-2016, 2016.

715 Fernald, F. G.: Analysis of atmospheric lidar observations: some comments, Applied optics, 23, 652–653, https://doi.org/10.1364/AO.23.000652, 1984.

Flynna, C. J., Mendozaa, A., Zhengb, Y., and Mathurb, S.: Novel polarization-sensitive micropulse lidar measurement technique, Optics express, 15, 2785–2790, https://doi.org/10.1364/OE.15.002785, 2007.

Freudenthaler, V.: About the effects of polarising optics on lidar signals and the Δ90 calibration, Atmospheric Measurement Techniques, 9,
720 4181–4255, https://doi.org/10.5194/amt-9-4181-2016, 2016.

Freudenthaler, V., Esselborn, M., Wiegner, M., Heese, B., Tesche, M., Ansmann, A., Müller, D., Althausen, D., Wirth, M., Fix, A., et al.: Depolarization ratio profiling at several wavelengths in pure Saharan dust during SAMUM 2006, Tellus B: Chemical and Physical Meteorology, 61, 165–179, https://doi.org/10.1111/j.1600-0889.2008.00396.x, 2009.

Garrett, T. J., Yuter, S. E., Fallgatter, C., Shkurko, K., Rhodes, S. R., and Endries, J. L.: Orientations and aspect ratios of falling snow,
725 Geophysical Research Letters, 42, 4617–4622, https://doi.org/10.1002/2015GL064040, 2015.

Griesche, H. J., Seifert, P., Ansmann, A., Baars, H., Barrientos Velasco, C., Bühl, J., Engelmann, R., Radenz, M., Zhenping, Y., and Macke, A.: Application of the shipborne remote sensing supersite OCEANET for profiling of Arctic aerosols and clouds during Polarstern cruise PS106, Atmospheric Measurement Techniques, 13, 5335–5358, https://doi.org/10.5194/amt-13-5335-2020, 2020.

Hajipour, M., Seifert, P., Griesche, H., Ohneiser, K., and Radenz, M.: Identification of multiple co-located hydrometeor types in Doppler
730 spectra from scanning polarimetric cloud radar observations, Atmospheric Measurement Techniques Discussions, 2024, 1–34, https://doi.org/10.5194/amt-2024-173, 2024.

He, Y., Liu, F., Yin, Z., Zhang, Y., Zhan, Y., and Yi, F.: Horizontally oriented ice crystals observed by the synergy of zenith-and slant-pointed polarization lidar over Wuhan (30.5° N, 114.4° E), China, Journal of Quantitative Spectroscopy and Radiative Transfer, 268, 107 626, https://doi.org/10.1016/j.jqsrt.2021.107626, 2021a.

He, Y., Yi, F., Yi, Y., Liu, F., and Zhang, Y.: Heterogeneous nucleation of midlevel cloud layer influenced by transported Asian dust over Wuhan (30.5° N, 114.4° E), China, Journal of Geophysical Research: Atmospheres, 126, e2020JD033 394, https://doi.org/10.1029/2020JD033394, 2021b.

Heymsfield, A. J. and Iaquinta, J.: Cirrus crystal terminal velocities, Journal of the atmospheric sciences, 57, 916–938, https://doi.org/10.1175/1520-0469(2000)057%3C0916:CCTV%3E2.0.CO;2, 2000.

Heymsfield, A. J. and Westbrook, C.: Advances in the estimation of ice particle fall speeds using laboratory and field measurements, Journal of the Atmospheric Sciences, 67, 2469–2482, https://doi.org/10.1175/2010JAS3379.1, 2010.

Hu, Y., Winker, D., Vaughan, M., Lin, B., Omar, A., Trepte, C., Flittner, D., Yang, P., Nasiri, S. L., Baum, B., et al.: CALIPSO/CALIOP cloud phase discrimination algorithm, Journal of Atmospheric and Oceanic Technology, 26, 2293–2309, https://doi.org/10.1175/2009JTECHA1280.1, 2009.

Jimenez, C., Ansmann, A., Engelmann, R., Donovan, D., Malinka, A., Schmidt, J., Seifert, P., and Wandinger, U.: The dual-field-of-view polarization lidar technique: a new concept in monitoring aerosol effects in liquid-water clouds – theoretical framework, Atmospheric Chemistry and Physics, 20, 15 247–15 263, https://doi.org/10.5194/acp-20-15247-2020, 2020.

Kajikawa, M.: Observations of the falling motion of plate-like snow crystals part I: the free-fall patterns and velocity, Journal of the Meteorological Society of Japan. Ser. II, 70, 1–9, https://doi.org/10.2151/jmsj1965.70.1_1, 1992.

Kikuchi, M. and Suzuki, K.: Characterizing vertical particle structure of precipitating cloud system from multiplatform measurements of A-Train constellation, Geophysical Research Letters, 46, 1040–1048, https://doi.org/10.1029/2018GL081244, 2019.

Kikuchi, M., Okamoto, H., and Sato, K.: A climatological view of horizontal ice plates in clouds: Findings from nadir and off-nadir CALIPSO observations, Journal of Geophysical Research: Atmospheres, 126, e2020JD033 562, https://doi.org/10.1029/2020JD033562, 2021.

Klett, J. D.: Orientation model for particles in turbulence, Journal of Atmospheric Sciences, 52, 2276–2285, https://doi.org/10.1175/1520-0469(1995)052%3C2276:OMFPIT%3E2.0.CO;2, 1995.

Klotzsche, S. and Macke, A.: Influence of crystal tilt on solar irradiance of cirrus clouds, Applied optics, 45, 1034–1040, https://doi.org/10.1364/AO.45.001034, 2006.

Kollias, P., Clothiaux, E., Miller, M., Albrecht, B., Stephens, G., and Ackerman, T.: Millimeter-wavelength radars: New frontier in atmospheric cloud and precipitation research, Bulletin of the American Meteorological Society, 88, 1608–1624, https://doi.org/10.1175/BAMS-88-10-1608, 2007.

Kolmogorov, A. N.: Dissipation of energy in the locally isotropic turbulence, Doklady Akademii Nauk SSSR, 32, 19–21, https://www.jstor.org/stable/51981, in Russian, 1941.

Lewis, J. R., Campbell, J. R., Stewart, S. A., Tan, I., Welton, E. J., and Lolli, S.: Determining cloud thermodynamic phase from the polarized Micro Pulse Lidar, Atmospheric Measurement Techniques, 13, 6901–6913, https://doi.org/10.5194/amt-13-6901-2020, 2020.

Li, H.: Growth and Melting of Atmospheric Ice Particles: Insights from Radar Observations, Ph.d. thesis, University of Helsinki, Helsinki, Finland, http://hdl.handle.net/10138/322859, 2021.

Li, H. and Moisseev, D.: Two layers of melting ice particles within a single radar bright band: Interpretation and implications, Geophysical Research Letters, 47, e2020GL087 499, https://doi.org/10.1029/2020GL087499, 2020.

Li, H., Möhler, O., Petäjä, T., and Moisseev, D.: Two-year statistics of columnar-ice production in stratiform clouds over Hyytiälä, Finland: environmental conditions and the relevance to secondary ice production, Atmospheric Chemistry and Physics, 21, 14 671–14 686, https://doi.org/10.5194/acp-21-14671-2021, 2021.

Li, J., Li, C., Zhao, Y., Li, J., and Chu, Y.: Geometrical constraint experimental determination of Raman lidar overlap profile, Applied Optics, 55, 4924–4928, https://doi.org/10.1364/AO.55.004924, 2016.

Li, J., Li, C., Guo, J., Li, J., Tan, W., Kang, L., Chen, D., Song, T., and Liu, L.: Retrieval of aerosol profiles by Raman lidar with dynamic determination of the lidar equation reference height, Atmospheric environment, 199, 252–259, https://doi.org/10.1016/j.atmosenv.2018.11.048, 2019a.

Li, J.-Z., Fan, S., Kopparla, P., Liu, C., Jiang, J. H., Natraj, V., and Yung, Y. L.: Study of terrestrial glints based on DSCOVR observations, Earth and Space Science, 6, 166–173, https://doi.org/10.1029/2018EA000509, 2019b.

Libbrecht, K. G.: The physics of snow crystals, Reports on progress in physics, 68, 855, https://doi.org/10.1088/0034-4885/68/4/R03, 2005.

Liou, K.-N. and Yang, P.: Light scattering by ice crystals: fundamentals and applications, Cambridge University Press, https://doi.org/10.1017/CBO9781139030052, 2016.

Marshak, A., Várnai, T., and Kostinski, A.: Terrestrial glint seen from deep space: Oriented ice crystals detected from the Lagrangian point, Geophysical Research Letters, 44, 5197–5202, https://doi.org/10.1002/2017GL073248, 2017.

Murray, F. W.: On the computation of saturation vapor pressure, Journal of Applied Meteorology and Climatology, 6, 203–204, https://doi.org/10.1175/1520-0450(1967)006%3C0203:OTCOSV%3E2.0.CO;2, 1967.

Neely, R. R., Hayman, M., Stillwell, R., Thayer, J. P., Hardesty, R. M., O'Neill, M., Shupe, M. D., and Alvarez, C.: Polarization lidar at Summit, Greenland, for the detection of cloud phase and particle orientation, Journal of Atmospheric and Oceanic Technology, 30, 1635–1655, https://doi.org/10.1175/JTECH-D-12-00101.1, 2013.

Nijhuis, A. O., Unal, C., Krasnov, O., Russchenberg, H., and Yarovoy, A.: Velocity-Based EDR Retrieval Techniques Applied to Doppler Radar Measurements from Rain: Two Case Studies, Journal of Atmospheric and Oceanic Technology, 36, 1693–1711, https://doi.org/10.1175/JTECH-D-18-0084.1, 2019.

Noel, V. and Chepfer, H.: A global view of horizontally oriented crystals in ice clouds from Cloud-Aerosol Lidar and Infrared Pathfinder Satellite Observation (CALIPSO), Journal of Geophysical Research: Atmospheres, 115, https://doi.org/10.1029/2009JD012365, 2010.

O'Connor, E. J., Illingworth, A. J., Brooks, I. M., Westbrook, C. D., Hogan, R. J., Davies, F., and Brooks, B. J.: A method for estimating the turbulent kinetic energy dissipation rate from a vertically pointing Doppler lidar, and independent evaluation from balloon-borne in situ measurements, Journal of atmospheric and oceanic technology, 27, 1652–1664, https://doi.org/10.1175/2010JTECHA1455.1, 2010.

Papetta, A., Marenco, F., Kezoudi, M., Mamouri, R.-E., Nisantzi, A., Baars, H., Popovici, I. E., Goloub, P., Victori, S., and Sciare, J.: Lidar depolarization characterization using a reference system, Atmospheric Measurement Techniques, 17, 1721–1738, https://doi.org/10.5194/amt-17-1721-2024, 2024.

Pruppacher, H. R. and Klett, J. D.: Microphysics of Clouds and Precipitation, Atmospheric and Oceanographic Sciences Library, Springer Dordrecht, Dordrecht, Netherlands, 2 edn., ISBN 978-0-7923-4211-3, https://doi.org/https://doi.org/10.1007/978-0-306-48100-0, 1996.

Radenz, M., Bühl, J., Seifert, P., Baars, H., Engelmann, R., Barja González, B., Mamouri, R.-E., Zamorano, F., and Ansmann, A.: Hemispheric contrasts in ice formation in stratiform mixed-phase clouds: disentangling the role of aerosol and dynamics with ground-based remote sensing, Atmospheric Chemistry and Physics, 21, 17969–17994, https://doi.org/10.5194/acp-21-17969-2021, 2021.

Ren, J., Tan, W., Tian, X., Wu, Z., Li, C., Li, J., Zhao, C., Liu, D., Kang, L., and Zhu, T.: Retrieval of aerosol liquid water content from high spectral resolution lidar, Science of The Total Environment, 799, 149423, https://doi.org/10.1016/j.scitotenv.2021.149423, 2021.

Ross, A., Holz, R. E., and Ackerman, S. A.: Correlations of oriented ice and precipitation in marine midlatitude low clouds using collocated CloudSat, CALIOP, and MODIS observations, Journal of Geophysical Research: Atmospheres, 122, 8056–8070, https://doi.org/10.1002/2016JD026407, 2017.

810 Saito, M. and Yang, P.: Oriented ice crystals: a single-scattering property database for applications to lidar and optical phenomenon simulations, Journal of the Atmospheric Sciences, 76, 2635–2652, https://doi.org/10.1175/JAS-D-19-0031.1, 2019.

Saito, M., Iwabuchi, H., Yang, P., Tang, G., King, M. D., and Sekiguchi, M.: Ice particle morphology and microphysical properties of cirrus clouds inferred from combined CALIOP-IIR measurements, Journal of Geophysical Research: Atmospheres, 122, 4440–4462, https://doi.org/10.1002/2016JD026080, 2017.

815 Sassen, K.: Remote sensing of planar ice crystal fall attitudes, Journal of the Meteorological Society of Japan. Ser. II, 58, 422–429, https://doi.org/10.2151/jmsj1965.58.5_422, 1980.

Sato, K. and Okamoto, H.: Refinement of global ice microphysics using spaceborne active sensors, Journal of Geophysical Research: Atmospheres, 116, https://doi.org/10.1029/2011JD015885, 2011.

Schimmel, W., Kalesse-Los, H., Maahn, M., Vogl, T., Foth, A., Garfias, P. S., and Seifert, P.: Identifying cloud droplets beyond lidar at-
820 tenuation from vertically pointing cloud radar observations using artificial neural networks, Atmospheric Measurement Techniques, 15, 5343–5366, https://doi.org/10.5194/amt-15-5343-2022, 2022.

Seifert, P.: Dust-related ice formation in the troposphere: A statistical analysis based on 11 years of lidar observations of aerosols and clouds over Leipzig, Ph.d. thesis, University of Leipzig, Leipzig, Germany, https://nbn-resolving.org/urn:nbn:de:bsz:15-qucosa-71167, 2011.

Seifert, P., Ansmann, A., Gross, S., Freudenthaler, V., Heinold, B., Hiebsch, A., Mattis, I., Schmidt, J., Schnell, F., Tesche, M., et al.: Ice
825 formation in ash-influenced clouds after the eruption of the Eyjafjallajökull volcano in April 2010, Journal of Geophysical Research: Atmospheres, 116, https://doi.org/10.1029/2011JD015702, 2011.

Stillwell, R. A., Neely III, R. R., Thayer, J. P., Shupe, M. D., and Turner, D. D.: Improved cloud-phase determination of low-level liquid and mixed-phase clouds by enhanced polarimetric lidar, Atmospheric Measurement Techniques, 11, 835–859, https://doi.org/10.5194/amt-11-835-2018, 2018.

830 Stillwell, R. A., Neely III, R. R., Thayer, J. P., Walden, V. P., Shupe, M. D., and Miller, N. B.: Radiative influence of horizontally oriented ice crystals over summit, Greenland, Journal of Geophysical Research: Atmospheres, 124, 12 141–12 156, https://doi.org/10.1029/2018JD028963, 2019.

Sun, X., Zhou, Y., Zhao, T., Fu, W., Wang, Z., Shi, C., Zhang, H., Zhang, Y., Yang, Q., and Shu, Z.: Vertical distribution of aerosols and association with atmospheric boundary layer structures during regional aerosol transport over central China, Environmental Pollution,
835 362, 124 967, https://doi.org/10.1016/j.envpol.2024.124967, 2024.

Takano, Y. and Liou, K.-N.: Solar radiative transfer in cirrus clouds. Part I: Single-scattering and optical properties of hexagonal ice crystals, Journal of Atmospheric Sciences, 46, 3–19, https://doi.org/10.1175/1520-0469(1989)046%3C0003:SRTICC%3E2.0.CO;2, 1989.

Tan, W., Zhao, G., Yu, Y., Li, C., Li, J., Kang, L., Zhu, T., and Zhao, C.: Method to retrieve cloud condensation nuclei number concentrations using lidar measurements, Atmospheric Measurement Techniques, 12, 3825–3839, https://doi.org/10.5194/amt-12-3825-2019, 2019.

840 Tan, W., Li, C., Liu, Y., Meng, X., Wu, Z., Kang, L., and Zhu, T.: Potential of Polarization Lidar to Profile the Urban Aerosol Phase State during Haze Episodes, Environmental Science and Technology Letters, 7, 54–59, https://doi.org/10.1021/acs.estlett.9b00695, 2020a.

Tan, W., Yu, Y., Li, C., Li, J., Kang, L., Dong, H., Zeng, L., and Zhu, T.: Profiling Aerosol Liquid Water Content Using a Polarization Lidar, Environmental Science Technology, 54, 3129–3137, https://doi.org/10.1021/acs.est.9b07502, 2020b.

Tansey, E., Marchand, R., Alexander, S. P., Klekociuk, A. R., and Protat, A.: Southern Ocean low cloud and precipitation phase ob-
845 served during the Macquarie Island Cloud and Radiation Experiment (MICRE), Journal of Geophysical Research: Atmospheres, 128, e2023JD039 205, https://doi.org/10.1029/2023JD039205, 2023.

Várnai, T., Kostinski, A. B., and Marshak, A.: Deep space observations of sun glints from marine ice clouds, IEEE Geoscience and Remote Sensing Letters, 17, 735–739, https://doi.org/https://doi.org/10.1109/LGRS.2019.2930866, 2019.

Vogl, T., Radenz, M., Ramelli, F., Gierens, R., and Kalesse-Los, H.: PEAKO and peakTree: Tools for detecting and interpreting peaks in cloud radar Doppler spectra–capabilities and limitations, Atmospheric Measurement Techniques, 17, 6547–6568, https://doi.org/10.5194/amt-17-6547-2024, 2024.

Wang, N., Zhang, K., Shen, X., Wang, Y., Li, J., Li, C., Mao, J., Malinka, A., Zhao, C., Russell, L. M., et al.: Dual-field-of-view high-spectral-resolution lidar: Simultaneous profiling of aerosol and water cloud to study aerosol–cloud interaction, Proceedings of the National Academy of Sciences, 119, e2110756 119, https://doi.org/10.1073/pnas.2110756119, 2022.

Wang, Z., Letu, H., Shang, H., Zhao, C., Li, J., and Ma, R.: A supercooled water cloud detection algorithm using Himawari-8 satellite measurements, Journal of Geophysical Research: Atmospheres, 124, 2724–2738, https://doi.org/10.1029/2018JD029784, 2019.

Wehr, T., Kubota, T., Tzeremes, G., Wallace, K., Nakatsuka, H., Ohno, Y., Koopman, R., Rusli, S., Kikuchi, M., Eisinger, M., et al.: The EarthCARE mission–science and system overview, Atmospheric Measurement Techniques, 16, 3581–3608, https://doi.org/10.5194/amt-16-3581-2023, 2023.

Welton, E. J. and Campbell, J. R.: Micropulse lidar signals: Uncertainty analysis, Journal of Atmospheric and Oceanic Technology, 19, 2089–2094, https://doi.org/10.1175/1520-0426(2002)019%3C2089:MLSUA%3E2.0.CO;2, 2002.

Westbrook, C., Illingworth, A., O'Connor, E., and Hogan, R.: Doppler lidar measurements of oriented planar ice crystals falling from supercooled and glaciated layer clouds, Quarterly Journal of the Royal Meteorological Society: A journal of the atmospheric sciences, applied meteorology and physical oceanography, 136, 260–276, https://doi.org/10.1002/qj.528, 2010.

Westbrook, C. D. and Illingworth, A. J.: Evidence that ice forms primarily in supercooled liquid clouds at temperatures>- 27 C, Geophysical research letters, 38, https://doi.org/10.1029/2011GL048021, 2011.

Whitehead, L. E., McDonald, A. J., and Guyot, A.: Supercooled liquid water cloud classification using lidar backscatter peak properties, Atmospheric Measurement Techniques, 17, 5765–5784, https://doi.org/10.5194/amt-17-5765-2024, 2024.

Xu, X., Jiang, Z., Li, J., Chu, Y., Tan, W., and Li, C.: Impacts of meteorology and emission control on the abnormally low particulate matter concentration observed during the winter of 2017, Atmospheric environment, 225, 117 377, https://doi.org/10.1016/j.atmosenv.2020.117377, 2020.

Yin, Z., Baars, H., Seifert, P., and Engelmann, R.: Automatic LiDAR calibration and processing program for multiwavelength Raman polarization LiDAR, in: EPJ Web of Conferences, vol. 237, p. 08007, EDP Sciences, https://doi.org/10.1051/epjconf/202023708007, 2020.

Yin, Z., Yi, F., He, Y., Liu, F., Yu, C., Zhang, Y., and Wang, W.: Asian dust impacts on heterogeneous ice formation at Wuhan based on polarization lidar measurements, Atmospheric Environment, 246, 118 166, https://doi.org/10.1016/j.atmosenv.2020.118166, 2021.

Yorks, J. E., Hlavka, D. L., Hart, W. D., and McGill, M. J.: Statistics of cloud optical properties from airborne lidar measurements, Journal of Atmospheric and Oceanic Technology, 28, 869–883, https://doi.org/10.1175/2011JTECHA1507.1, 2011.

Zhang, K., Wu, L., Rosenfeld, D., Müller, D., Li, C., Zhao, C., Landulfo, E., Jimenez, C., Wang, S., Hu, X., Li, W., Li, X., Sun, Y., Liu, S., Wu, L., Wan, X., Chen, W., Liu, C., Bai, J., Li, J., Sun, W., Venkataraman, S., Zhou, Y., Deng, Z., Liu, M., Cheng, M., Fu, Z., Pan, W., and Liu, D.: Simultaneous Retrieval Algorithm of Water Cloud Optical and Microphysical Properties by High-Spectral-Resolution Lidar, IEEE Transactions on Geoscience and Remote Sensing, 62, 1–11, https://doi.org/10.1109/TGRS.2024.3416493, 2024.

Zhao, C., Wang, Y., Wang, Q., Li, Z., Wang, Z., and Liu, D.: A new cloud and aerosol layer detection method based on micropulse lidar measurements, Journal of Geophysical Research: Atmospheres, 119, 6788–6802, https://doi.org/10.1002/2014JD021760, 2014.

Zhou, C., Yang, P., Dessler, A. E., Hu, Y., and Baum, B. A.: Study of horizontally oriented ice crystals with CALIPSO observations and comparison with Monte Carlo radiative transfer simulations, Journal of Applied Meteorology and Climatology, 51, 1426–1439, https://doi.org/10.1175/JAMC-D-11-0265.1, 2012a.

Zhou, C., Yang, P., Dessler, A. E., and Liang, F.: Statistical properties of horizontally oriented plates in optically thick clouds from satellite observations, IEEE Geoscience and Remote Sensing Letters, 10, 986–990, https://doi.org/10.1175/JAMC-D-11-0265.1, 2012b.

885